ABSTRACT

CRYSTALLOGRAPHIC STRUCTURE AND MECHANICAL PROPERTIES OF TANTALUM COATINGS ON STEEL DEPOSITED BY DC MAGNETRON SPUTTERING

by

Charanjeet Singh Paur

Tantalum metal exhibits excellent erosion and corrosion resistance property. Hence, tantalum coatings are investigated for protection of steel surface exposed to mechanical stresses, high temperature, and corrosive environment. Such conditions exist inside large army gun barrels. The goal of this work was to contribute to the development of technology for tantalum coating of steel, which would replace the presently used electrochemical chromium deposition. A DC magnetron sputtering process was used to deposit tantalum coatings on steel substrates. In sputtering, tantalum is deposited in two phases: ductile, body-centered cubic (bcc) phase (α-phase) and a metastable, brittle tetragonal β-phase. Only α-phase of tantalum is considered suitable for protective coatings. Such coatings were successfully deposited on steel substrates heated to 400°C (with Ar sputtering gas) and 350°C (with Kr), and also at room temperature if tantalum nitride interlayers were first deposited on steel substrates. Tantalum phase composition was determined by x-ray diffraction (XRD). The crystallographic phase of the nitride interlayer, studied by XRD, and its composition measured by the nuclear reaction analysis, showed that the stoichiometric TaN is required for α-phase deposition. Adhesion of sputter deposited tantalum coatings was evaluated using a scratch test method. It was found that strongly adhering α-phase tantalum coatings can be deposited on sputter etched steel substrate with tantalum nitride interlayer, and also on substrates heated to elevated temperatures. Adhesion failure of coatings was different for the ductile α-phase or predominantly α-phase coatings, and the brittle β-phase coatings, which under an optical microscope revealed numerous small cracks, before delamination. This study confirms the superiority of the α-phase tantalum over β-phase tantalum in protective coating applications. Parameters of DC magnetron sputtering deposition process for obtaining α-phase tantalum coatings were also determined.

CRYSTALLOGRAPHIC STRUCTURE AND MECHANICAL PROPERTIES OF TANTALUM COATINGS ON STEEL DEPOSITED BY DC MAGNETRON SPUTTERING

by
Charanjeet Singh Paur

A Thesis
Submitted to the Faculty of
New Jersey Institute of Technology
in Partial Fulfillment of the Requirements for the Degree of
Master of Science in Materials Science and Engineering

Interdisciplinary Program in Materials Science and Engineering

August 2002

APPROVAL PAGE

CRYSTALLOGRAPHIC STRUCTURE AND MECHANICAL PROPERTIES OF TANTALUM COATINGS ON STEEL DEPOSITED BY DC MAGNETRON SPUTTERING

Charanjeet Singh Paur

Dr. Marek Sosnowski, Thesis Advisor Date
Associate Professor, Department of Electrical and Computer Engineering, NJIT.

Dr. Ken Chin, Committee Member Date
Director, Materials Science and Engineering M.S./Ph.D. Program, NJIT.

Dr. Roumiana Petrova, Committee Member Date
Special Lecturer, Department of Physics, NJIT.

BIOGRAPHICAL SKETCH

Author: Charanjeet Singh Paur

Degree: Master of Science

Date: August 2002

Undergraduate and Graduate Education:

- Master of Science in Materials Science and Engineering
  New Jersey Institute of Technology, Newark, NJ, 2002

- Bachelor of Engineering in Metallurgical Engineering
  Maharaja Sayajirao University, Baroda, India, 1999

Major: Materials Science and Engineering

Presentations and Publications:

Anamika Patel, Leszek Gladczuk, Charanjeet Singh Paur, Marek Sosnowski, "Sputter-deposited bcc tantalum on steel with the interfacial tantalum nitride layer," *Materials Research Society Symposium Proceedings,* vol. 697, P5.6, 2002.

Anamika Patel, Charanjeet Singh Paur, Leszek Gladczuk, Marek Sosnowski, "Control of crystalline phase of tantalum deposited on steel by magnetron sputtering," *The Electrochemical Society Journal* (submitted), Spring 2002.

Charanjeet Singh Paur, Anamika Patel, Chirag Joshi, Leszek Gladczuk and Marek Sosnowski, "Effect of sputtering parameters on the phase of tantalum coatings deposited on steel," *13th annual Sigma Xi Student Research Symposium,* St. Joseph's University Chapter of Sigma Xi, Philadelphia, April 2002.

To my dear Dad-Mom, Bhaiya-Bhabhi, Happy and Little Heman

ACKNOWLEDGEMENT

I would like to express my sincerest gratitude to Professor Marek Sosnowski, who not only served as my research advisor, providing valuable guidance and intuition, but also constantly gave me his concern and encouragement. I would like to express my appreciation to Dr. Ken Chin and Dr. Roumiana Petrova for serving as members on the thesis committee and for their invaluable inputs.

I had the pleasure of working with my colleagues - Anamika Patel, Cheng Li, Chirag Joshi and especially, Leszek Gladczuk at the Ion Beam and Thin Film Laboratory at NJIT. Their help and suggestions are appreciated and acknowledged. I would like to extend my appreciation to my roommates Ravi, Amit and Nikunj and, fellow graduate students, who supported me, at the most needed moments and made my stay at NJIT more memorable.

Finally, I will be always grateful to my parents, brothers, sister-in-law, my adorable nephew – Heman and, old pals Viral and Ankoor for their support, encouragement and love. This work would not have been possible without them.

TABLE OF CONTENTS

TABLE OF CONTENTS
(Continued)

TABLE OF CONTENTS
(Continued)

LIST OF TABLES

LIST OF FIGURES

LIST OF FIGURES
(Continued)

LIST OF FIGURES
(Continued)

LIST OF FIGURES
(Continued)

CHAPTER 1

INTRODUCTION

The main goal of this work was to study and evaluate the sputtering process parameters necessary to yield body-centered cubic α-phase tantalum coatings on steel substrate. Factors affecting the adhesion of tantalum coatings were also studied.

1.1 Properties and Applications of Tantalum

Tantalum metal has many applications in mechanical systems, electronics, biomedical field and others. In electronics, tantalum and tantalum nitride have been used for many years in manufacturing of capacitors and resistors. Since the advent of Cu interconnects for deep sub-micron multilevel integrated circuits, Ta has become a highly promising diffusion barrier material for copper interconnects in integrated circuits [1], polish stop and adhesion layer for chemical mechanical polishing (CMP) of the damascene process [2]. Furthermore, Ta and nitrided tantalum or tantalum alloyed with nitrogen (Ta-N) thin films are effective diffusion barriers to prevent the highly diffusing Cu from reacting with the underlying silicon and surrounding SiO_2 dielectric. Thus, the growth of Ta and TaN thin film on SiO_2 has been extensively studied, particularly in terms of controlling the phase, electrical property and microstructure of the Ta and TaN films so that they can be used as reliable barriers between Cu and Si/SiO_2. Physical properties of tantalum metal, like high melting point (2996°C), good ductility (bcc-phase), elastic modulus similar to steel and low thermal conductivity; and chemical properties like inertness in corrosive environments, make it a suitable material for erosion and corrosion-resistant coatings on steel subjected to elevated temperatures, pressures and stresses [3]. Tantalum nitride is a potential candidate for wear resistant coatings on high-speed steels (HSS) [4,5]. Excellent corrosion resistance, chemical stability and histo-compatibility of tantalum explain its use as a biomedical material in orthopedics since the 1940s. Spur in recent studies on the surface modification of blood-contacting biomaterials brought tantalum nitride into focus due to its superlative corrosion and wear resistance and higher hardness than TiN (conventionally used surface coatings on biomaterials) [6].

Tantalum has two distinct crystallographic phases. A body-centered cubic (bbc) α-phase is characteristic of bulk Ta and has physical properties making it desirable for gun tube coating applications. A second, metastable, tetragonal β-phase, which was first observed in sputtered Ta films, is hard and brittle, thermally unstable, and transforms to the bcc phase at temperatures above 750°C [7]. Some of the physical and electrical properties of both the phases have been listed in the Table 1.1 below [8].

Table 1.1 Properties of Tantalum

Tantalum phase	Theoretical Density gm/cc	Resistivity μΩ.cm	Crystal structure and lattice parameter
Bulk tantalum	16.55	13	bcc a=3.303 Å
Sputtered α-Ta	16.27-16.55	24-50	bcc a=3.31-3.33 Å
Sputtered β-Ta	16.90	180-220	tetragonal a=5.313 Å c=10.194 Å

1.2 Tantalum for Protective Coatings

The motivation of a large study on tantalum coatings, of which this research project is a part, was to develop a process for protective bore coating of medium and large caliber military gun tubes. Conventionally, chromium coatings were electrochemically deposited from aqueous solution, to protect the inner surfaces of gun tubes. However, Cr (VI), formed in the chromium salt solution during the electrolytic deposition process, is hazardous to health (carcinogenic) and toxic waste disposal is a problem [2]. Sputtering of tantalum is an environmentally friendly and clean process, and there is no known health hazard associated with tantalum.

Tantalum is also being considered as a replacement for chromium because of its superior performance. Tantalum is more refractory than chromium (melting point: 1860°C), has a relatively lower thermal conductivity (57 W/m°C Vs. 91 W/m°C for Cr at 20°C), is much more ductile than electrodeposited high contractile (HC) chromium, making it far less susceptible to crack formation and subsequent coating failure in gun tube applications.

Tantalum protective coatings can be deposited from fused salt baths or by chemical vapor deposition technique [9,10]. However, both these methods involve high temperatures, above 800°C, and these temperatures exceed the tempering temperature of the substrate steel and hence adversely affect the mechanical properties of the steel itself. To avoid degradation of the gun tube mechanical properties, tantalum coatings are applied to liners, which are shrunk fit into the gun tube. This process can be avoided if the protective coating could be applied directly to the gun tube surface at temperatures less than about 500°C. High rate sputtering is a technique, which can be used to deposit thick metallic coatings in a reasonable time, at substrate temperatures significantly below 500°C [11].

For tantalum coating to be a good protective barrier, it should be continuous with few defects and adhere well to the substrate it intends to protect. Vapor-deposited Ta coatings are often found to contain one or both crystalline phases, viz. α-phase and β-phase. The pressure on brittle β-phase can lead to film cracking. The β-phase transformation to stable α-phase at high temperatures produce stresses, leading to delamination and subsequently, failure of the coating during service. Therefore, means and process parameters were studied to generate pure α-Ta coatings on steel substrate.

1.3 Literature Review

As pointed out in Section 1.2, tantalum has been deposited as thin films as well as thick coatings. The division is somewhat arbitrary and here, layers with thickness < 5 μm are called films and thicker ones are coatings; the recent literature review is divided into two parts, accordingly. The following paragraph reviews the literature on tantalum as thin films, while latter paragraph will be focused on studies related to thick tantalum coatings for erosion and corrosion protection.

The ability to control α- and β-phase tantalum nucleation and growth is highly desirable for coatings and thin film applications. Shimada et al. [12] showed that low-resistivity (~15 μΩ.cm), α-tantalum layer was stably self-grown on TaN_x buffer layer on SiO_2 due to hetero-epitaxy by sputtering even if the ion energy is maintained at low levels such as 10 eV, although only high resistivity (~160 μΩ.cm) β-tantalum phase is ordinarily formed by a conventional sputtering method on silicon and oxidized silicon substrates, in CMOS technology. Philippe Catania et al. [13] reported that at zero bias voltage on substrate the films produced had bcc phase, while increasing the bias to –100 V, increases the resistivity dramatically, and induces formation of β-Ta, with no significant change in film impurity levels. Clevenger et al. at IBM concluded that the main stress relief mechanism for tantalum films with intrinsic compressive stresses to completely relax their stress is the beta-to-alpha phase transition, while for intrinsically tensile films, this transformation has a much smaller effect on the stress [14].

Matson et al. [15] reported sputtered α-tantalum on cylindrical bore surfaces with a triode sputtering apparatus. It was seen that by introducing a niobium interface layer strongly effected the phase composition in the tantalum layer resulting in pure α-phase. Lee et al. [16] studied the phase, texture and stress in the coatings with Nb-interlayer. They recommended optimization of deposition parameters to control phase composition, impurity contents, residual stress level, texture and microstructure to further improve coating behavior. In yet another study, Matson et al. [7,17] tried to summarize the results of investigations into the effects of sputtering gas species, substrate temperature and substrate bias during the deposition process on the phase composition and distribution in the thick sputtered Ta coatings. They showed that elevated substrate temperatures (between 200°C and 300°C) and the use of heavier sputtering gases were conducive to the formation of α-Ta phase sputtered on 4340 steel substrates in the cylindrical triode sputtering geometry. Different researchers reported contradictory results, on effect of substrate biasing on phase composition of tantalum films and coatings. Whereas, Matson et al. had reported that higher substrate biases (-110 V to -150 V) appeared to have less β-phase.

CHAPTER 2

SPUTTERING

2.1 Deposition Techniques

For many decades, substrate surfaces have been coated using physical and chemical vapor deposition techniques. The physical vapor deposition (PVD) processes involve controllable transfer of atoms or molecules from a source to a substrate, where film formation and growth proceeds. The two basic PVD methods used for thin film or coating deposition are evaporation and sputtering. In evaporation, atoms are removed from the source by thermal means, whereas in sputtering they are dislodged from a solid target (source) surface through impacts of gaseous ions. Chemical vapor deposition (CVD) is the process of chemically reacting a volatile compound of a material to be deposited, with other gases, to produce a non-volatile solid that deposits atomistically on a suitably placed substrate [18].

2.2 Plasma

Due to aforementioned reasons (Section 1.2), sputtering was employed to deposit tantalum coatings on steel in our studies. Therefore, an effort is made in this chapter to explain sputtering in general, and dc magnetron sputtering in particular. Sputtering being a process utilizing plasma, arises a question in the mind - what is plasma?

Plasma is defined as a partially ionized gas (typically 0.001 % to 10 % of the available atoms and molecules), containing an equal number of positively and negatively charged particles. This permits current to flow through the gas medium, making the gas conductive. At room temperature, a plasma or glow discharge can be initiated and sustained between two electrodes with a sufficiently high voltage difference, placed in a gaseous environment at a pressure in the medium vacuum range (≤ 1 torr). This condition, often called the fourth state of matter, is characterized by a visible glow and increased electric conductivity. The glow is caused by the relaxation of excited gas atoms, in which an electron makes a transition from a higher to a lower energy state, emitting energy in the form of visible light, characteristic of that gas.

2.3 Mechanism of Sputtering

As shown in Figure 2.1, when an energetic ion impinges on the surface of a solid (target) one or all of the following phenomena may occur:

- The ion may become implanted or be reflected, probably as a neutral and probably with a large loss of energy.
- The impact may cause the target atom to emit a secondary electron.
- The ion impact and the resulting collision cascade may cause an amount of structural reordering in the surface layers of the target.
- The ion impact may set up a series of collisions between atoms of the target, leading to the ejection of one of the target atoms. This ejection process is known as sputtering.

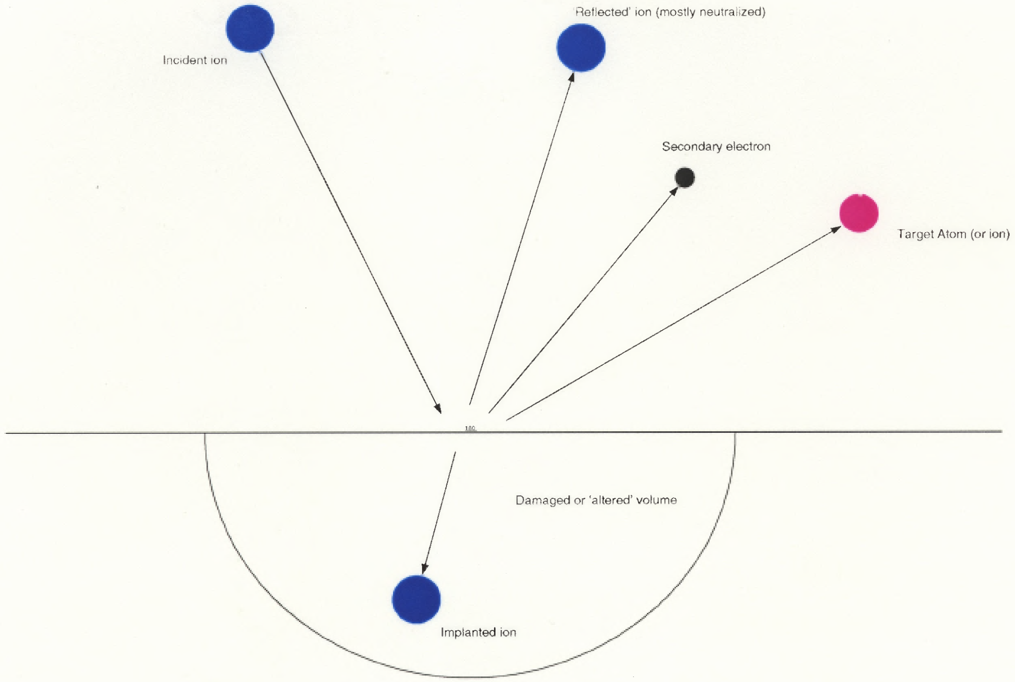

Figure 2.1 Interactions of ions with surfaces [19].

In the energy range most relevant to sputter deposition, the interaction between the impinging ion and the target atoms, and the subsequent interactions amongst the latter, can be treated as a series of binary collisions. The sputtering process is very often compared to the break in a game of atomic billiards (Figure 2.2) in which the cue ball (the bombarding ion) strikes the neatly arranged pack (the atomic array of the target), scattering balls (target atoms) in all directions, including some that move back towards the player, i.e. out of the target surface. In the real process, the interatomic potential function (the variation of interatomic repulsion or attraction with separation distance) is rather different from the hard sphere billiard ball case, but nevertheless the billiard model is instructive [19].

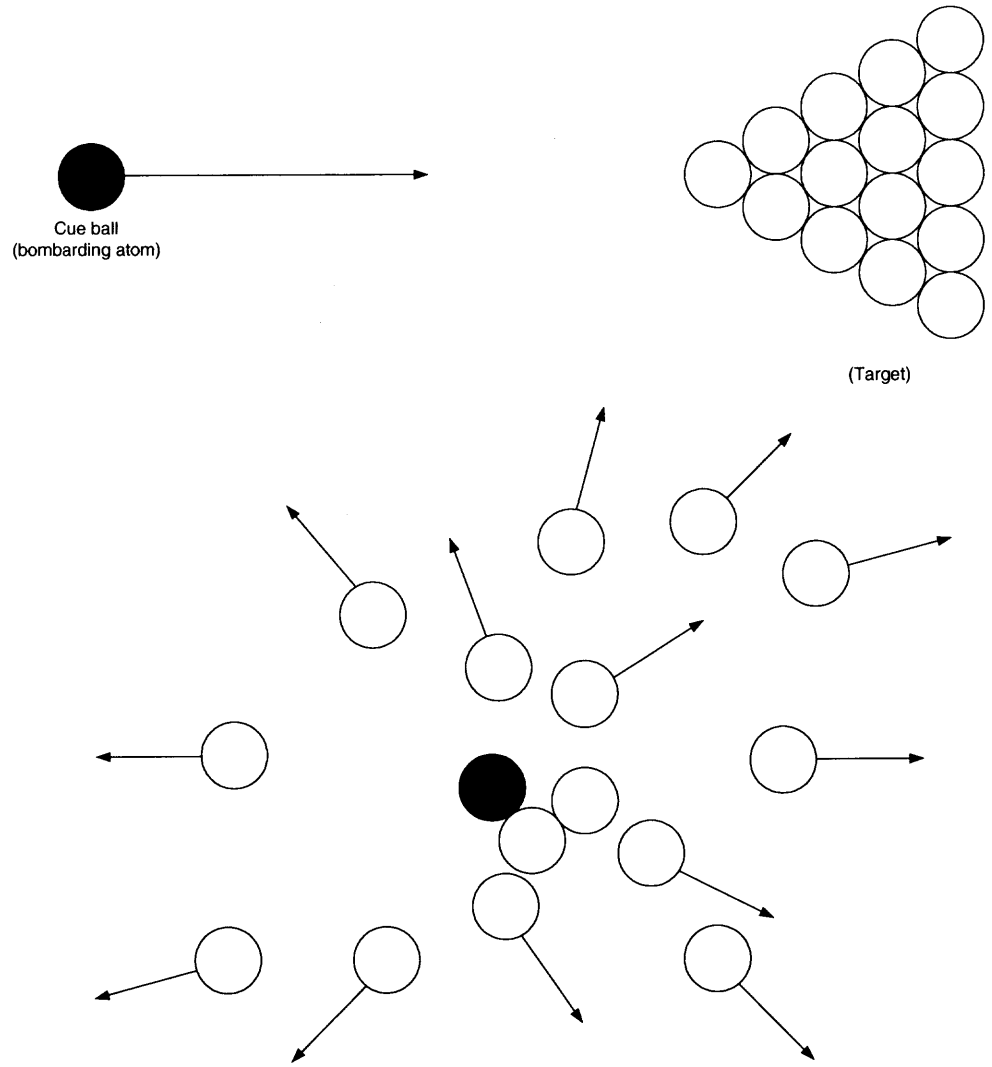

Figure 2.2 Sputtering – the atomic billiards game [19].

A formal definition of sputtering can be given as, a process that involves knocking an atom or molecule out of a target material by accelerated ions from an excited plasma and condensing it on the substrate either in its original or in a modified form. When this modification is induced by a chemical reaction during the transit from the target to the substrate or at the surface of the substrate or target, the process is referred to as reactive sputtering. The resulting coating is held firmly to the surface by Van der Waals forces, although, in some cases, an alloy or chemical bond may result.

Sputtering has proven to be a successful method of coating a variety of substrates with thin films of electrically conductive or non-conductive materials. One of the most striking characteristics of sputtering is its universality. Since the coating material is transferred in the form of atoms or molecules by ion impacts rather than a chemical or thermal process, virtually any material can be deposited. Direct current is used to sputter conductive materials (DC sputtering), while radio frequency is used for non-conductive materials (RF sputtering). The range of sputtering application is large.

2.4 Sputtering Modes

Ultra-thin films to thick coatings of target material can be deposited by sputtering on to the substrate surface. The planar sputtering configuration is used to coat plane substrates in VLSI and ULSI fabrication and cylindrical sputtering apparatus is used to deposit coatings on cylindrical surface areas like inside of gun barrels for corrosion and erosion protection. A wide variety of coatings of pure elements, alloys and compounds can be deposited on variety of substrates with reactive or non-reactive sputtering process.

Depending on the various modes to accelerate plasma ions onto the target material, sputtering is basically classified into four types:

1. DC sputtering
2. RF sputtering
3. Bias sputtering
4. Ion beam sputtering

2.4.1 DC Sputtering

A DC sputtering system basically consists of two electrodes, cathode and anode placed in an evacuated chamber. The schematic of such a system is shown in Figure 2.3. A high negative DC voltage is applied to the cathode (sputtering target), whereas anode (substrate) is either grounded, electrically floating or is biased positively or negatively. Inert gas, generally argon is introduced in the chamber at some specific pressure. The interaction between the electric field (generated between the two electrodes) and the sputtering gas produces glow discharge. Positive ions generated in the plasma are accelerated towards the target and impinge on it. During these interactions momentum transfer from the ions to the target atoms cause the ejection of latter. The sputtered atoms from the target fly off in random directions, and some of them land on the substrate, condense there, and form a thin film. The main disadvantage of this technique is that it cannot sputter non-conductive materials.

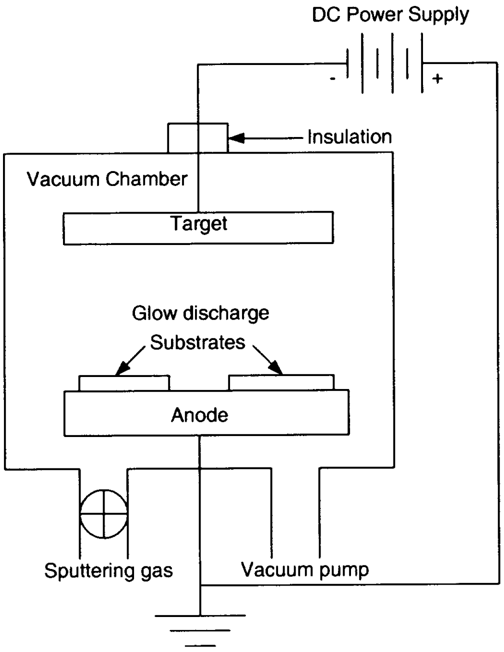

Figure 2.3 Schematic of a DC sputtering system [18].

2.4.2 RF Sputtering

Radio frequency sputtering was invented as a means of depositing insulating thin films, since they cannot be deposited by DC sputtering technique due to requirement of unattainable potential differences between the cathode and anode. Some nominal insulators could be sputtered by dc sputtering technique, but it is not usually a very good solution because of problems such as stress developed in the target due to resistive heating. The technique of RF sputtering uses an alternating voltage power supply at RF frequencies above 10 MHz, so that the sputtering target is alternately bombarded by ions and then electrons so as to avoid charge build-up. A schematic diagram of a RF sputtering system is shown in Figure 2.4.

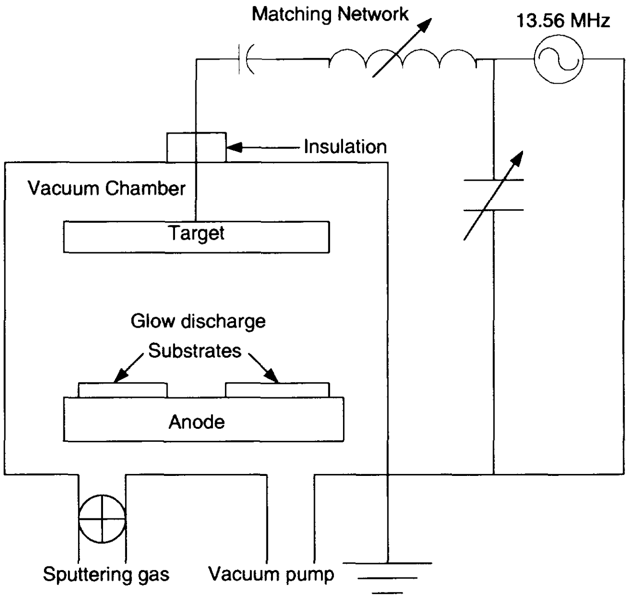

Figure 2.4 Schematic of a simplified RF sputtering system [18].

Another advantage of RF sputtering over DC sputtering is unlikeliness of arcing, which is sometimes a problem in DC sputtering systems. Arcing can be due to patches of dirt (with higher secondary electron coefficient), pockets of outgassing (higher pressure, higher current density locally), or asperities (higher electric field strength). These arcs are less likely to form in RF discharges because the field is maintained in one direction for less than one cycle, and reduces to zero twice in each cycle, making it more difficult for the arc to be sustained [19].

2.4.3 Bias Sputtering

With so many particles bombarding the film, and with the sensitivity of the nucleation and growth processes to this bombardment, one would expect to be able to influence the properties of the film by changing the flux and energy of incident particles. It is difficult to directly modify the behavior of the neutral particles, but the charged particles can be controlled by changing the local electric field, and this is the basis of the technique of bias sputtering [19]. In this technique, electric fields near the substrate are modified in order to vary the flux and energy of incident charged species. Generally a negative DC or RF bias is applied to the substrate. With target voltages of –1000 V to –3000 V, bias voltages of –50 V to –300 V are typically used. This technique has been successfully used in all sputtering configurations (DC, RF, magnetron and reactive). It has also been found that biasing can alter a wide range of properties like resistivity, hardness and residual stress, dielectric properties, etch rate, optical reflectivity, step coverage, film morphology, density and adhesion [18].

2.4.4 Ion Beam Sputtering

This technique employs a noble gas ion beam, extracted from the ion source, to bombard a target as shown in Figure 2.5. The target can be used as a sputter deposition source to coat a substrate; this process is variously known as ion beam sputter deposition, secondary ion beam deposition (although the depositing material is unionized), and ambiguously as ion beam deposition.

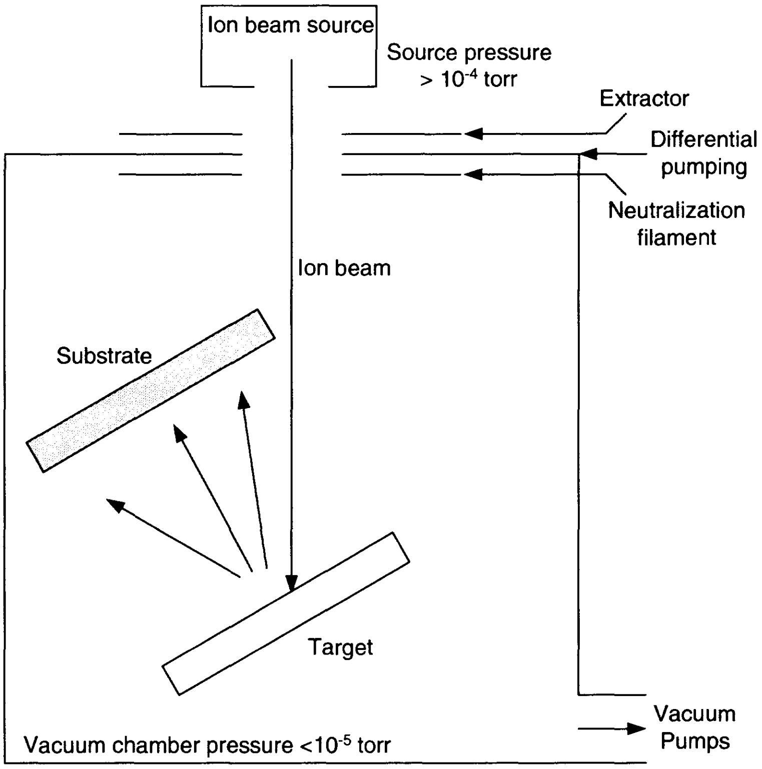

Figure 2.5 Typical configuration for ion beam sputtering [19].

The advantages of such sputtering are [19],

- Due to isolation of the substrates from the glow discharge generation process, unwanted heating of the substrates and fast electron bombardment are minimized.
- Since the substrates are not part of the electrical circuit, it is much easier to incorporate substrate heating, cooling and process controls.
- The low operating pressure in the process chamber minimizes gas contamination of the growing film.

- The low operating pressure also reduces energy-attenuating collisions of the sputtered particles en route from target to substrate.

2.5 Magnetron Sputtering

In a conventional DC sputtering system, a major source of charged particle bombardment at the substrate is due to electrons. With a conducting substrate, the average current density is about 1mA/cm^2, which is equivalent to $6.25 \text{ X } 10^{15}$ electrons/cm^2.sec or a few electrons for each depositing atom. The majority of these electrons are thermal electrons from the glow where they have energies of a few electron volts, but in addition to these slow electrons, there is bombardment by fast electrons, emitted from the target by ion and other impacts. These fast electrons can have a major influence on the structure and properties of the growing film on the substrate. The large energy input causes a good deal of substrate heating, and there are more subtle effects due to the electron interaction with the surface.

Also, it is seen that the range of operating pressure for a DC diode system is limited due to lack of electron impact ionization to sustain the discharge. There are two ways to combat this limitation, either by increasing the probability of ionization or by increasing the number of electrons. This can be achieved by following means,

- Using a magnetic field to increase the path length of an electron before it is collected or recombines on an electron or wall.
- Using the ionization enhancement give by RF excitation.
- Injecting more electrons into the discharge by using a hot filament as an electron source.

Magnetron sputtering systems exploit the magnetic field effect to take advantage of the first method listed above. These systems have advantages in sputtering rate (current densities at the target are 10-100 mA/cm^2, compared to about only 1 mA/cm^2 for DC diode configurations), extend ability of operating range (can sustain a glow discharge at much lower pressures), and can reduce electron bombardment at the substrate. The problems of deposition uniformity, which sometimes arise, can be overcome in many cases.

Principles of Magnetron Sputtering

The process can be described by considering the motion of an electron having charge q, mass m_e and velocity v. If the electron is moving in a region of uniform magnetic field B (into the paper in Figure 2.6 (a)) and zero electric field, it experiences a force F perpendicular to both, the direction of its motion and the direction of B. It can be stated in mathematical equation as under,

$$F = q\,(v \times B) \tag{2.1}$$

This force produces an acceleration that is inversely proportional to the mass of the charge. For the magnetic fields used in sputtering, which are typically 100 gauss, only the electrons will be affected; the ions are too massive. The electron, under the influence of this force F will describe a semicircle of radius r, provided it does not collide en route, and return to the surface with velocity v, whose value is given by the following equation,

$$r = m_e v/qB \tag{2.2}$$

So the effect of the magnetic field is to trap the electron near the surface from which it was emitted.

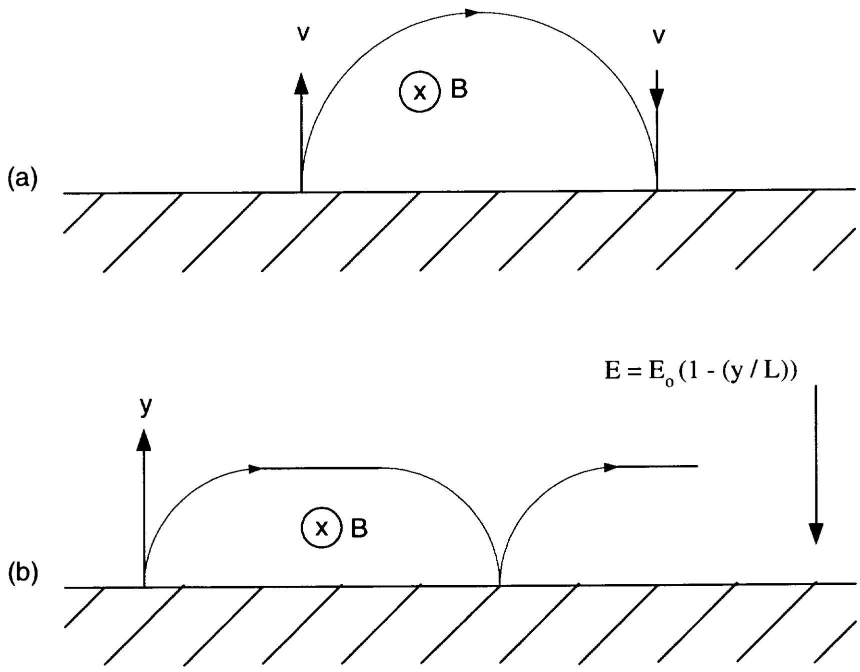

Figure 2.6 Motion of an electron ejected from a surface with velocity v into a region of magnetic field B parallel to the surface: (a) with no electric field, and (b) with a linearly decreasing field [19].

Figure 2.6 (b) represents a more realistic situation in a magnetron system, where a strong electric field E decrease linearly across the dark space of thickness L above the cathode (target) surface and a magnetic field B is parallel to the surface of the target as in previous case. If y is the dimension away from the target and the target surface is y = 0, then

$$E = E_0 (1 - (y/L)) \tag{2.3}$$

where, E_0 is the electric field at the target.

Considering the equation of motion for the electron, assuming its emission velocity to be zero, we can derive the following equation,

$$y = qE_o/m_e\omega^2(1-\cos\omega t) \qquad (2.4)$$

where, $\omega^2 = qE_o/m_eL + q^2B^2/m_e^2$.

In the absence of the electric field, ω would be equal to qB/m_e. This is known as the cyclotron frequency and has the value $2.8 \times 10^6 B$ Hz, where B is in gauss. In the absence of the emitting surface, the electron would rotate around the field lines with the cyclotron frequency. The addition of the electric field on the target changes the orbits from circular to cycloidal. The instantaneous radius of curvature will decrease according to the above equation as it travels further from the target surface. If it enters the negative glow by straying further than L from the target, then it will describe circular motion in the electric field-free region there, before undergoing a collision with a gas particle.

The net result of all this is that the electron is trapped near the target provided it does not make any collisions, so the loss process of fast electrons going to the anode and walls is eliminated. If it does make collisions, the trapping would not be effective, but on the other hand we want the electrons to make lots of ionizing collisions to sustain the glow, and the magnetron action enables them to do this before being lost to the anode.

2.6 Reactive Sputtering

In reactive sputtering, thin films of compounds are deposited on substrates by sputtering from metallic targets in the presence of a reactive gas, usually mixed with the inert working gas (generally Ar). The most common compounds reactively sputtered (and the reactive gases employed) are briefly listed below [18]:

- Oxides (oxygen) – Al_2O_3, In_2O_3, SnO_2, SiO_2, Ta_2O_5
- Nitrides (nitrogen, ammonia) – TaN, TiN, AlN, Si_3N_4
- Carbides (methane, acetylene, propane) – TiC, WC, SiC
- Sulphides (Hydrogen sulphide) – CdS, CuS, ZnS
- Oxycarbides and oxynitrides of Ti, Al, Ta and Si

Irrespective of which of these materials is considered, during reactive sputtering the resulting film is either a solid solution alloy of the target metal doped with the reactive element (e.g., $TaN_{0.01}$), a compound (e.g., TiN), or some mixture of the two.

The most critical problem related with reactive sputtering is target poisoning, in which the oxygen or nitrogen react with parts of the metallic target. The dielectric that forms on the target surface is sputtered extremely slowly, leading to low deposition rates. In more critical situations, target poisoning interrupts the normal sputtering process of the target and leads to instabilities like sparks and plasma extinguishing. The remedy for this problem is to lower the concentration of reactive element in the working gas atmosphere and increase pumping rate of the chamber.

CHAPTER 3

SURFACE PREPARATION OF SUBSTRATE

Two kinds of alloy steels, viz. 4340 steel and gun steel were used as substrates for tantalum coating deposition. The chemical composition of these steels is shown in Table 3.1.

Table 3.1 Chemical Composition of AISI-SAE 4340 Steel and Gun Steel [20, 21]

Element	AISI-SAE 4340 Alloy Steel (wt. %)	Gun Steel (wt. %)
Carbon	0.36-0.44	0.37
Manganese	0.55-0.80	0.47
Silicon	0.15-0.30	0.02
Chromium	0.60-0.90	0.85
Nickel	1.65-2.00	3.17
Molybdenum	0.20-0.30	0.65
Vanadium	-	0.10
Phosphorus	0.035 max	0.006
Sulphur	0.040 max	0.01

The surface preparation of the substrate was divided into three steps, viz. mechanical cleaning (machining, grinding, abrasion and polishing), electrochemical cleaning and ultrasonic cleaning in solvents.

3.1 Mechanical Cleaning

The steel was cut into small square pieces of 0.5" X 0.5" size and thickness 0.2" using conventional machine shop practice at NJIT. The surface of the steel substrates was subjected to grinding, abrasion and polishing, all employing an array of fixed abrasive particles whose projecting points act as the cutting tools. The manner in which the abrasives are supported on a backing material and the speed at which the material is removed decides whether the process is grinding, abrasion or polishing.

In grinding, the abrasives are cemented together into a rigid block whose exposed surface is the working surface. This surface is 'dressed' by fracturing the exposed abrasive particles to form an array of sharp points. Examples are cutoff wheels, grinding wheels, abrasive laps and abrasive stones. After cutting the steel samples, grinding was done on 60-grit size grinding wheel.

Abrasion generally employs a layer of abrasive particles cemented onto a cloth or paper backing, creating coated abrasive products such as papers, clothes or belts. In some processes, abrasive particles are embedded in a comparatively soft material, thus producing an array of abrasive points, for example lapping wheels. Surface speed employed can be further used to distinguish between grinding and abrasion. Grinding is done at high surface speeds and significant heating of the surface layers take place due to the friction between the two surfaces. Abrasion employs comparatively lower speeds and liquid coolant; hence heating of the specimen surface is avoided.

Polishing uses abrasive particles that are not firmly fixed but suspended in a liquid among the fibers of a cloth. The objective is to produce a bright, mirror-like reflecting surface, commonly referred to as a polished surface.

Typical metallographic preparation procedures employ a sequence of machining or grinding stages of increasing fineness, then a sequence of abrasion process of increasing fineness, followed by a sequence of polishing processes of increasing fineness until the desired surface finish has been achieved. Increasing fineness refers to the use of finer grades of abrasive to produce finer grooves or scratches in the surface.

In grinding and abrasion, the abrasive points can be compared with V-point cutting tools having a wide range of rake angles. Only a small proportion of these abrasives are at the right angle to cut off a metal chip, whereas others just plough through the specimen surface displacing material laterally. In both cases scratches are produced and severe plastic deformation of the surface layer of the specimen occurs. Most mechanical polishing procedures are similar to those for abrasion, except that only small forces are applied to individual abrasive particles by the fibers of the cloth that supports them. They, therefore, produce comparatively shallow and narrow scratches. Thus, the processes involved in grinding, abrasion and polishing differ in degree rather than in kind [22].

The surface preparation operations can be done manually or can be mechanized. In manual preparation, after the preliminary machining and grinding the specimen is rubbed on the abrasive material supported on a flat backing surface in one direction till all previous scratches are removed and the new scratches are oriented in one direction. The surface is then rotated 90° and the above-mentioned step is repeated, using successively finer grades of abrasive paper, usually to the finest available. Water is used as a coolant as well as a lubricant in grinding and abrasion steps. It also flushes out the abrasion debris as they form. Waterproof abrasive papers, usually those coated with silicon carbide abrasive are convenient for this purpose.

The surface is then polished by holding the specimen over a high speed rotating polishing wheel, which is charged with a fine abrasive suspended in an appropriate carrier liquid. The polishing wheel consists of a polishing cloth stretched across a flat backing surface. Several stages of polishing employing increasingly finer abrasives usually are necessary. Diamond, alumina (Al_2O_3) and magnesium oxide (MgO) are the abrasives most commonly used for polishing; colloidal silica is sometimes used. The specimen should be thoroughly washed after each operation to remove any foreign particle or debris from the previous polishing step, which could be carried on to next operation and produce some unwanted scratches.

Mechanized processes are less time consuming and laborious than the manual operations. Automation is particularly useful if large numbers of specimens have to be prepared. Practice and experimentation are the only ways to come up with the right surface preparation procedure. Once the optimum preparation parameters are established, the results can be reproduced exactly without having to rely on the operator. In this method, a variably loaded mechanical arm in lieu of a hand is used to move the specimen in a unique geometric pattern (Figure 3.1) against the abrasive paper or polishing cloth. The steps involved in mechanized process are same as in manual process explained above. The specimen should be held and rotated so that the section surface is maintained precisely in a horizontal plane against the working surface of the abrasive or polishing wheel.

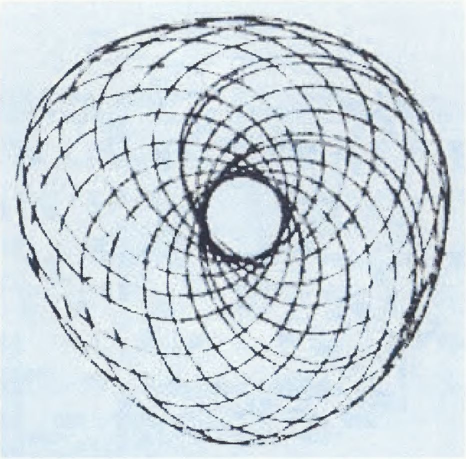

Figure 3.1 Pattern produced by MINIMET polishing action [23].

Figure 3.2 MINIMET 1000 Grinder/Polisher.

MINIMET 1000 Grinder/Polisher (Buehler Company) was used for steel substrate surface preparation (Figure 3.2). It is a highly automated machine, providing control of rotation speeds (variable from 3.5 cm/s to 35 cm/s, in increments of 3.5 cm/s), pressure applied to the specimen (variable from 5 to 50 N in increments of 5 N) and polishing time (up to 99 minutes at a time). The adhesive-backed abrasive carrier is applied on to a glass platen and this glass platen is kept inside a bowl to avoid coolant (water) spillage from the abrasive around the machine. The sequence and optimum grinding and polishing parameters established for preparation of our steel substrates are shown in Table 3.2 and Table 3.3.

Table 3.2 Grinding Process and Parameters

Abrasive, Size, average particle size	Abrasive carrier	Lubricant	Load	Speed (cm/s)	Time
SiC,240 grit,54 μm	Emery paper	DI water	30-40 N	17.5-24.5	4-5 min
SiC,320 grit, 36 μm	Emery paper	DI water	30-40 N	17.5-24.5	4-5 min
SiC,400 grit, 24 μm	Emery paper	DI water	30-40 N	17.5-24.5	4-5 min
SiC,600 grit, 16 μm	Emery paper	DI water	30-40 N	17.5-24.5	4-5 min

Table 3.3 Polishing Process and Parameters

Abrasive, Size	Abrasive carrier **	Lubricant	Load	Speed (cm/s)	Time
Diamond, 15 μm	Kempad	-	25-35 N	21-28	5-6 min
Diamond, 10 μm	Kempad	-	25-35 N	21-28	5-6 min
Diamond, 6 μm	Kempad	-	25-35 N	21-28	5-6 min
Diamond, 3 μm	Kempad	-	25-35 N	21-28	5-6 min
Diamond, 1 μm	Kempad	-	25-35 N	21-28	5-6 min
Diamond, 0.5 μm	Kempad	-	25-35 N	21-28	5-6 min
Alumina suspension, 0.05 μm	Vel-cloth	DI water	45-0 N *	17.5-35 *	2 min

* For the 0.05 μm final polish the load is gradually decreased from 45 N to minimum load and speed is gradually increased from 17.5cm/s to 35 cm/s in 2 minutes.

** Kempad and Vel-cloth are tradename products of Allied High Tech Products, Inc.

3.2 Electrochemical Cleaning

After the mechanical method for surface polishing, electrochemical cleaning or electrolytic cleaning was employed to clear the steel substrate of any impurities like oil, grease, dirt, rust, fingerprints, etc. As the name suggests, electrochemical cleaning is an electrolytic method utilizes two electrodes in an electrolyte, connected to a power supply. The schematic of an electrochemical cleaning setup is shown in Figure 3.3.

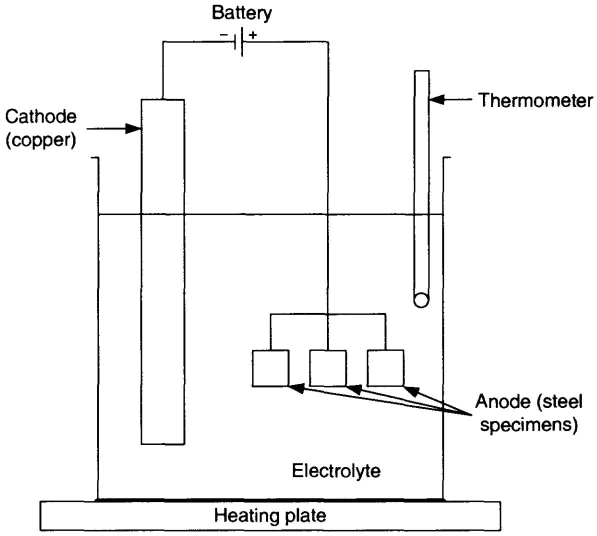

Figure 3.3 Schematic of an electrochemical cleaning setup.

Electrochemical cleaning can be classified as anodic (if the specimen to be cleaned is made the anode) or cathodic (if the specimen to be cleaned is connected as the cathode). The two processes differ with respect to the type of gas evolved at the specimen electrode when current flows through the electrolytic cell.

In case of anodic electrochemical cleaning process, also called as reverse current cleaning, oxygen is liberated on the anode as a result of the following reaction,

$$2OH^-_{(aq)} \rightarrow H_2O_{(l)} + \frac{1}{2} O_{2(g)} + 2e^- \qquad (3.1)$$

For the cathodic process of cleaning a specimen, which is made the cathode in the cell, insoluble steel or nickel-plated steel anodes are used. The chemical reaction at the specimen electrode is

$$2H^{+}_{(aq)} + 2e^{-} \rightarrow H_{2\,(g)} \qquad (3.2)$$

The oxygen and hydrogen gas liberated at the electrodes create a scrubbing action, which actually blasts dirt particles off the work piece. These bubbles rise to the top of the cleaner, agitating the solution and continually bringing fresh cleaning solution to the work. Anodic cleaning is mostly used for ferrous metals, while cathodic method is good for certain alloys, such as nickel that are easily passivated by oxides, if cleaned anodically [24].

In this study, anodic electrochemical cleaning was carried out on the steel substrates in 'Electrocleaner 59 Special', an alkaline solution, which is a proprietary product of Northwest Company. The solution chemistry and operating conditions used for the procedure were as under:

Anode: Steel substrates to be cleaned

Cathode: Copper

Concentration of the electrolyte: 60-75 g/l (of distilled water)

Temperature: 71-93°C

Voltage: 6-8 V

Current density: 30-50 mA/cm^2

Cleaning time: 15 minutes

Finally, the electrochemically cleaned samples were rinsed in DI water to remove any residual alkaline cleaner, before subjecting them to ultrasonic cleaning.

Besides steel substrates, tantalum coatings were deposited on silicon substrate and oxidized silicon substrate. The goal was to study the effect of different substrates on the depositing tantalum phases. Also, as resistivity measurement (four-point probe method) of tantalum coating is compromised by the low resistivity of steel (substrate), these measurements were done on Si and SiO_2 substrates. Small pieces (about 0.6" X 0.6") of silicon and silicon dioxide substrates were cut from wafers used for electronic applications. As the wafers were highly polished, they did not need any further polishing operation. Their smoothness and flatness facilitated an accurate thickness measurement by mechanical profilometry method explained in Chapter 5.

Si and SiO_2 along with steel substrates were subjected to ultrasonic cleaning as a final cleaning step before putting the samples inside the sputtering chamber.

3.3 Ultrasonic Cleaning

Ultrasonic cleaning is done in liquid medium, using high frequency sound waves (~ 33,000 Hz), which create millions of micro bubbles traveling at ultrasonic speeds through the medium. These bubbles surrounding all surfaces of the work piece to be cleaned, implode on them, reaching pressures up to 1000 bar causing dirt to be lifted from the surface.

The steel, Si and SiO_2 substrates were subjected to three cycles of ultrasonic cleaning. Firstly, the specimens were ultrasonically cleaned in alcohol for ten minutes, then for five minutes in acetone and finally, ten more minutes in alcohol again. After all these cleaning operations, the samples were preserved in a desiccator to prevent any chemical reactions on the clean surface of the substrates with the atmospheric air before placing them in the sputtering chamber for deposition.

CHAPTER 4

SPUTTERING SYSTEM AND PROCEDURE

Tantalum coatings were deposited on steel substrate using a planar DC magnetron sputtering apparatus. The sputtering system was designed and assembled at the Ion Beam and Thin Film Laboratory at NJIT, while the main parts were fabricated and supplied by Kurt J. Lesker Company.

4.1 Sputtering System

The sputtering system consists of a cylindrical chamber, 20" inside diameter and 15" height. The total volume of the chamber is approximately 80 liters. A photograph of the DC planar magnetron sputtering system in the Ion Beam and Thin Film Laboratory at NJIT is shown in Figure 4.1.

The system is equipped with a CRYO-TORR 8 high vacuum pump (CTI-Cryogenics, Helix Technology Corporation) and two turbo molecular pumps, viz. Turbovac 150 and Turbovac 50 (Leybold-Heraeus) and two rotary mechanical pumps (Leybold-Heraeus) to back-up the turbo pumps. The pumping assembly is able to evacuate the chamber to vacuum pressures below 1 X 10^{-7} torr. The high vacuum pressure inside the chamber was measured with an ionization gauge whereas the low pressure developed by mechanical pump alone is measured by a thermocouple vacuum gauge. Turbovac 50 pump with the backing rotary pump from Leybold-Heraeus was used for pumping the residual gas analyzer (RGA). The RGA (Inficon Quadrex-200 Model from Leybold-Heraeus) was connected to the sputtering chamber through a throttling valve and was capable of analyzing the chamber gas composition continuously during deposition. The schematic of the gas flow and pumping system is shown in Figure 4.2.

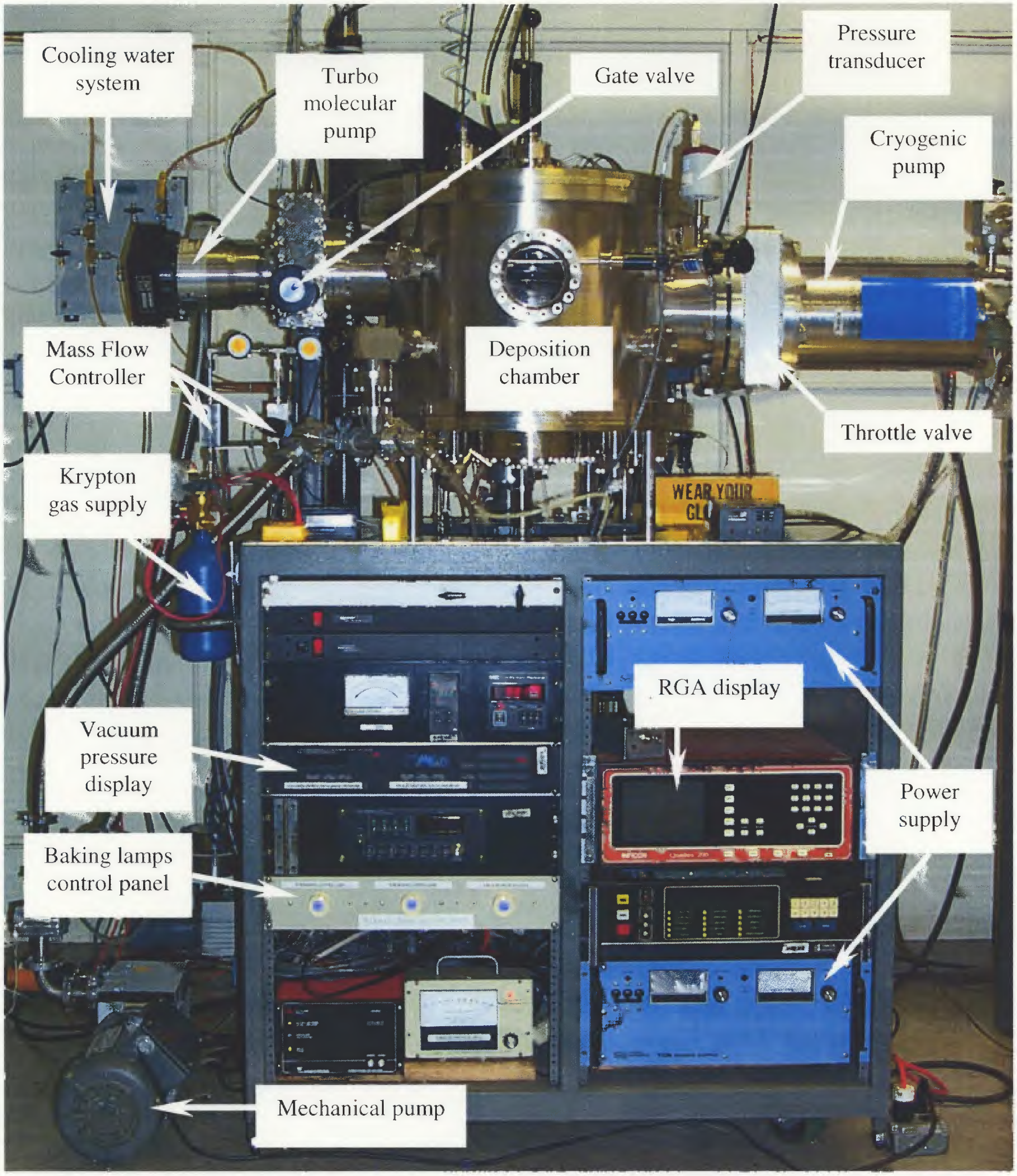

Figure 4.1 Planar DC magnetron sputtering system at NJIT.

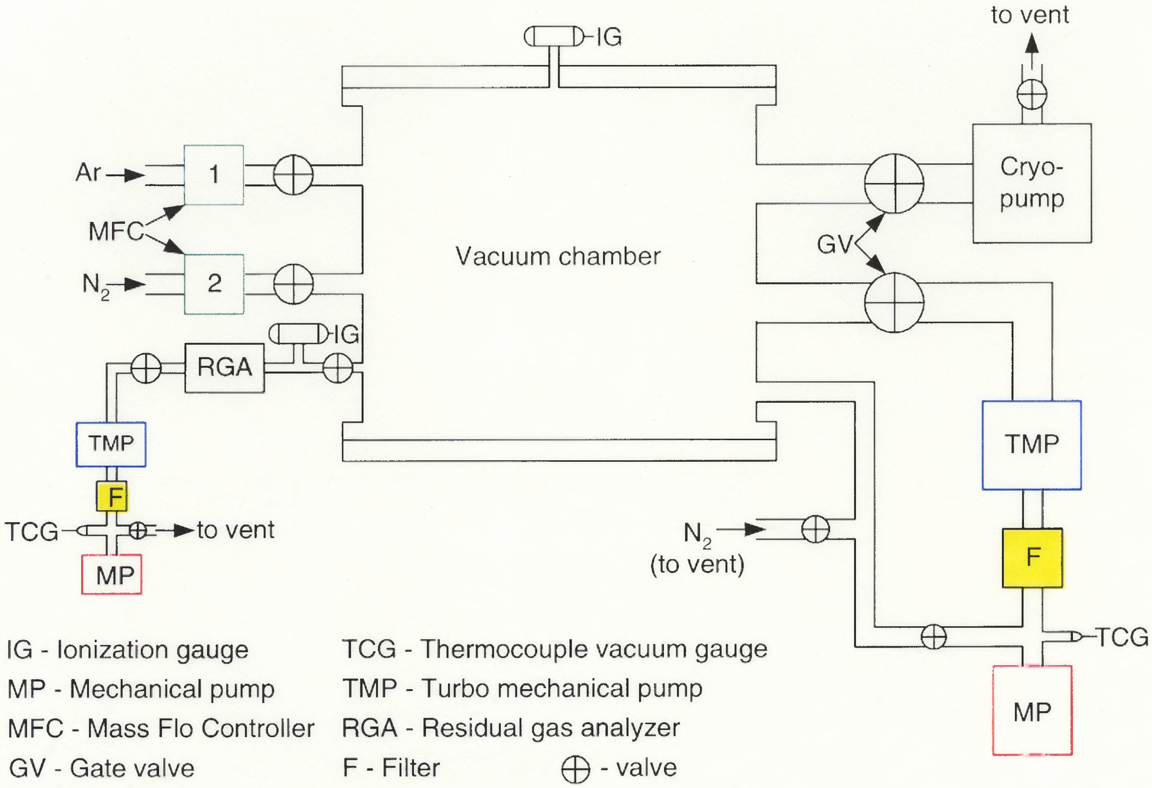

Figure 4.2 Schematic of the vacuum and gas flow control of the deposition chamber.

The outgassing from the chamber walls and other parts inside the chamber produced a noticeable amount of residual gases, especially water vapor, which made it desirable to bake the chamber. Baking under vacuum to about 200°C for 6-8 hours was done with two elongated type halogen lamps (500 W, 120 V) placed inside the chamber, one vertical in the lower half and the other one is parallel to and near the lid of the chamber (Figure 4.3). After baking, the chamber is cooled down overnight before sputtering.

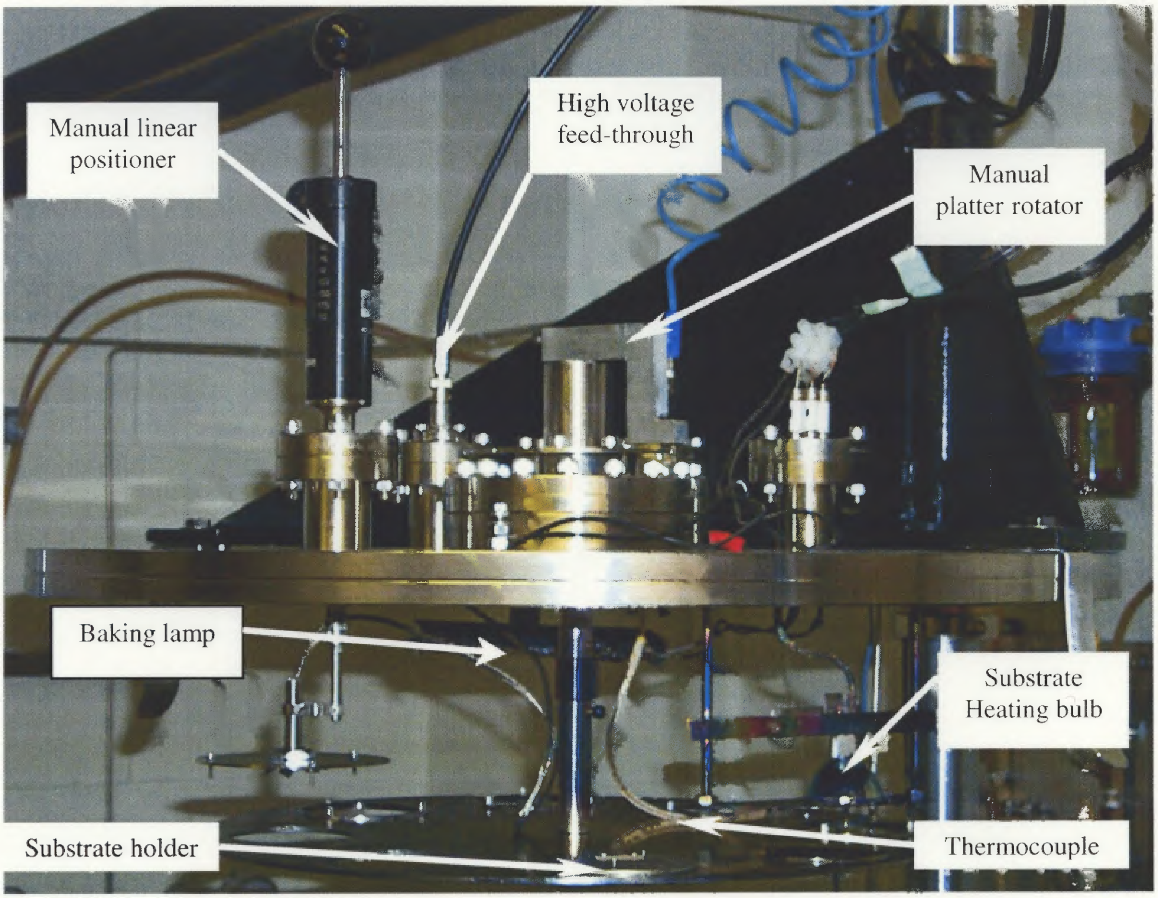

Figure 4.3 Setup of the vacuum chamber lid.

The substrates to be sputtered upon were mounted on a circular 2.75” diameter, substrate mounting plate (substrate holder) by 4-40 screws as seen in Figure 4.4. Eight of such substrate holders can be placed in turn on a round rotating substrate platter, which was suspended from a vertical shaft in the center of the lid of the chamber. The distance between the substrates and the target was set to 2 inches. The manual rotation of the platter was facilitated from the top of the chamber by a rotary feed-through as seen in Figure 4.3. The platter was so designed that only one substrate holder at a time is sputtered upon. Although, more than one sputtering source could be mounted on the base of chamber, this study employed only one source for sputtering. To avoid unnecessary coating of the chamber walls with the target material, a circular stainless steel shield supported on four poles was introduced under the substrate platter, above the sputtering source. Also, a shutter (a thin stainless steel plate) was provided just on top of the source to close the window in the shield above the source. In case of plasma being extinguished in middle of deposition, the shutter was pulled over to prevent deposition on the substrates before stabilizing the process parameters inside the chamber.

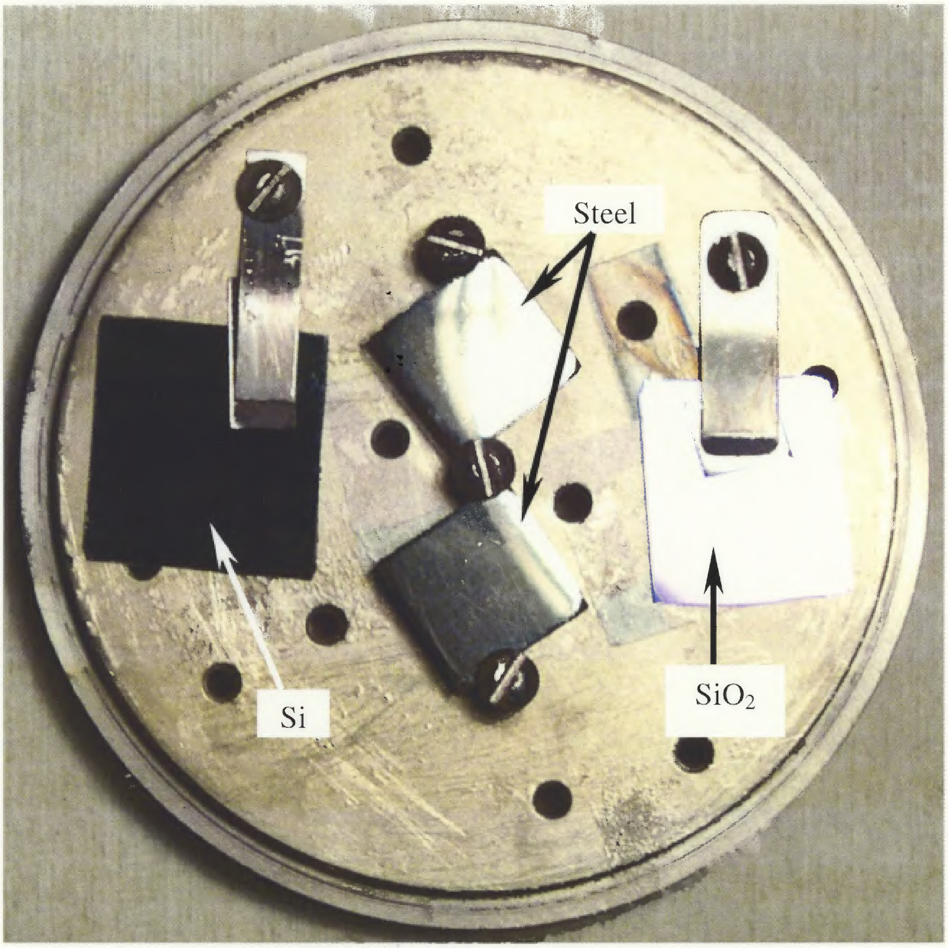

Figure 4.4 Substrates mounted on a holder.

The tantalum target (99.9998 % purity) of 2" diameter and 0.125" thickness was obtained from Electronic Space Products International Company. It was mounted in the TORUS 2A Magnetron sputtering source obtained from Kurt J. Lesker Company. The rating of this kind of source was [25]:

Sputtering power: 1 KW DC
Cathode voltage: 200 - 900 V (peak)
Discharge current: 0 - 3 A
Operating pressure: 5 - 200 millitorr

A DC power supply (0-1600 V DC, 0-1.5 A DC) was used for deposition. In some experiments requiring higher current during deposition, another DC power supply (0-600 V DC, 0-5 A DC) was used. Due to the high power generated in the target during sputtering, sufficient water cooling (0.5 gallon/minute) of the source is necessary to prevent the target from overheating and damaging the permanent magnets of the source.

The ultra high purity working (sputtering) gases, viz. argon (99.999 %), krypton (99.998 %) and nitrogen (99.999 %) were passed into the sputtering chamber through the mass flow controllers (MKS Instruments) at a specific rate. Nitrogen gas was used for reactive sputtering along with argon. The working pressure inside the chamber is measured by a pressure transducer (MKS Baratron model Type 626) with a range from 0.1 millitorr to 1 torr.

As known from literature, sputtering tantalum on substrates maintained at elevated temperatures yielded bcc-phase Ta. Hence heating of the substrates while sputtering was accomplished by placing a halogen lamp (300 W, 120 V) inside the chamber, above the substrate holder (see Figure 4.3). The substrate can be heated up to

400°C using this lamp connected through a 0-120 VAC variac, which is isolated from the system via a 1:1 isolation transformer.

4.2 Sputter Etching

The adhesion of a film to the substrate can be improved by cleaning the substrate surface in situ, so that the film and substrate atoms really come close. Since vacuum deposition is an atomistic or molecular process, this is a real possibility, unlike the contact of two bulk materials. Solvent cleaning usually removes only oils and greases, leaving more tenacious materials such as surface oxides. One can remove such deposits by chemical or sputter etching. In situ sputter etching is preferred than doing it in a separate chamber, because exposure to the atmosphere after sputter etching, while transferring the substrates to the deposition chamber, can re-oxide the surface or a least cover it with some foreign molecules by physio-adsorption.

Sputter etching is the name conventionally given to the process of removal of material from a surface by sputtering. Sputter etching can be carried out in a conventional sputtering system with glow discharge plasma, or with an externally generated ion beam. Surface cleaning can be done in glow discharges by placing the substrates to be cleaned in the plasma so that they are bombarded by low energy ions and electrons. Although glow discharge cleaning is effective for removing much contamination, it is ineffective in removing the native oxide layers or other compounds from metal or semiconductor surfaces. This can be done by sputter etching in which the material being cleaned is made the target of a sputtering system. The discharge could be RF or DC, with the former required for insulating materials. In both cases, the target is exposed to energetic ions and, in the RF case, also to low energy electrons [19]. In contrast to glow discharge cleaning, sputtering causes removal of the surface contaminants and target atoms too. However, this cleaning method is known to have some negative effects on substrates, which includes redeposition, change of surface morphology (cone formation) and some surface contamination due to impacts of sputtering gas ions [26].

In this study, the substrates and substrate holders were sputter etched inside the sputtering chamber in argon glow discharge by making them cathodes (by supplying negative potential to them). Sputter etching was done after baking and cooling the chamber (to minimize residual gas content), but prior to coating deposition as described in next section. Typical DC voltage used for sputter etching was in the range of 300-400V at a working pressure of 180-230 mtorr when argon was flown into the chamber at 18 sccm. The sputter etching current measured was ranging from 0.5-1.5 mA and corresponding calculated current density was 10-40 $\mu A/cm^2$. The sputter etching time varied from 10-60 minutes on each substrate holder. In some cases, a ceramic substrate holder was used with substrates mounted from the back. Advantage of such a holder and mounting method was that redeposition on the substrates from the mounting screws and the holder itself can be avoided. The setup for the sputter etching can be viewed in Figure 4.3. Adhesion test of coatings deposited on sputter-etched substrates is discussed in Chapter 7.

4.3 Deposition Procedure

1. Substrates for deposition are prepared as explained in Chapter 3.
2. The sputtering chamber is opened up. Condition of the target is judged; chamber parts like substrate platter, substrate holders, shields, shutter, etc. are thoroughly cleaned to prevent any loosely sticking films on these parts to peel off and drop down on the target and produce sparks or short in the system.
3. The cleaned steel, Si and SiO_2 samples are mounted on the substrate holder and then these holders are loaded inside the chamber (Figure 4.5).
4. Chamber is pumped overnight by the cryogenic pump to pressure of about 4×10^{-7} torr.

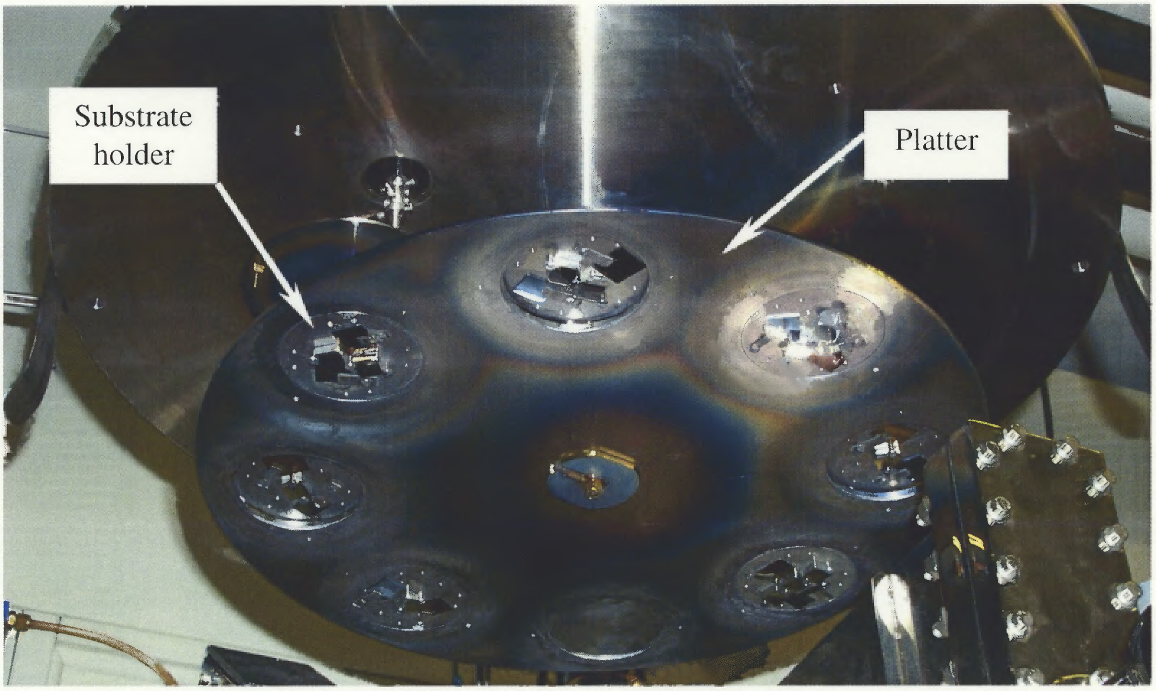

Figure 4.5 Platter loaded with sample holders.

5. Next day the chamber is baked at about 200°C for 6-8 hours and then left to cool down overnight.
6. The vacuum obtained after baking and then pumping over night is $1 \text{ X } 10^{-7}$ torr or lower.
7. The gate valve to the cryogenic pump is fully closed. The Turbovac 150 pump is started and its gate valve to the chamber is opened partially (see Figure 4.2).
8. Working gases are passed through the chamber at a predetermined flow rate and the gate valve is adjusted for the desired process gas pressure.
9. Sputter etching is carried out on selected substrate holders.
10. Before films are sputtered, the target is conditioned for 10-15 minutes by sputtering on a blank plate (with no samples) to remove any native oxide film or any impurity atom adsorbed on the target surface.
11. Tantalum nitride films are deposited by reactive sputtering in nitrogen and argon atmosphere on selected substrates.
12. Tantalum coatings are deposited, with or without heating on the nitride layer or on bare substrates. The working parameters used in the aforementioned steps are varied a lot and they will be discussed in the Chapter 7.

After the whole deposition process is completed, the samples are usually left inside the chamber overnight. The next day the chamber is vented with high purity (99.998 %) nitrogen gas and samples are taken out for analysis.

CHAPTER 5

CHARACTERIZATION TECHNIQUES

This chapter discusses the experimental techniques associated with determination of,

1. Film thickness
2. Film morphology and structure
3. Film composition

Although, there are many characterization methods for thin films and coatings, the author will only discuss some of the techniques used by him to analyze the tantalum coatings. Profilometry was used for the determination of film thickness. Film morphology and structure were analyzed by X-ray diffraction, optical microscopy and scanning electron microscopy. The chemical characterization was done in order to identify surface and interior atoms and compounds, as well as their lateral and depth spatial distributions. Nuclear reaction analysis was employed for the elemental analysis of the films.

The three aforementioned aspects represent the common core of information required of all films and coatings irrespective of ultimate application. Beyond these broad characteristics, there are a host of individual properties, viz. adhesion, electrical conductivity, stress, hardness and others, that are specific to the particular application. The adhesion of the film to the substrate is tested by a scratch test method, which is discussed in detail in Chapter 6. This chapter discusses only the basic principles underlying the characterization methods mentioned above. The results obtained from these techniques will be discussed in Chapter 7.

5.1 Profilometry

Stylus-method profilometry was used to measure the thickness of the films using DEKTAK IIA surface profile measuring system, from Veeco Instruments Inc. In this technique the mechanical movement of a diamond tipped stylus with a tip radius of 12.5 μm is measured to trace the topography of a film-substrate step. The stylus force is adjustable from 1 to 40 mg, and vertical magnifications of a few thousand up to a million times are possible. Film thickness is directly read out as the height of the resulting step-contour trace. The leveling and measurement functions are computer-controlled. The vertical stylus movement is digitized, and the data can be processed to magnify areas of interest and yield best profile fits. Calibration profiles are available for standardization measurements. The scan distances range from 0.05 mm to 30 mm with a vertical resolution of 5 Å [18].

5.2 X-Ray Diffraction

The phenomenon of x-ray diffraction by crystals results from a scattering process in which x-rays are scattered by the electrons of the atoms without change in wavelength (coherent or Bragg scattering). A diffracted beam is produced by such scattering only when certain geometrical conditions are satisfied, which are given by Bragg's equation as under:

$$n\lambda = 2d\sin\theta \tag{5.2}$$

where, n = integral number describing the order of reflection,

λ = wavelength of the x-rays,

d = interplanar spacing for the reflecting plane, and

θ = Bragg angle where a maximum in the diffracted intensity occurs.

X-ray diffraction yields information about the crystal structure, including lattice constants and geometry, identification of unknown materials, orientation of single crystals, and preferred orientation of polycrystals, defects, stresses, etc. [18].

The instrumentation required for X-ray powder diffractometry consists of three basic parts:

1. A source of radiation, consisting of an X-ray tube and a high-voltage generator
2. The detector and counting instrument
3. The diffractometer

Since the powder diffraction pattern of a material is a characteristic of that substance, comparison of the diffraction data obtained from an unknown material can be compared with the standard Powder Diffraction Files (PDF) of thousands of known materials compiled by the Joint Committee on Powder Diffraction Standards (JCPDS), to know its chemical composition, crystallinity and other properties. The data on each powder diffraction file is classified on the basis of the three most intense diffraction lines. The file also contains for each pattern the spacing between the crystallographic planes, d, for every line and the relative intensities of the lines based on the strongest line as 100 [27].

5.3 Microscopy

Features of a sample can be examined by reflection of some form of radiation from the surface. The optical microscopy uses visible light as radiation and image is magnified by proper optical system (microscope). It is usually necessary to first treat the surface by some physical and/or chemical process that alters the way light is reflected by the various structural constituents that are of interest. In scanning electron microscopy, the radiation used is a highly focused beam of electrons, revealing the sample microstructure by the way the electrons are reflected off the surface. Both these techniques are discussed in little more detail in the following section.

5.3.1 Optical Microscopy

Optical microscope is the simplest microscopy tool that can be used to see microscopic features of metallic specimen. By careful surface preparation of the specimen like polishing and then etching with a suitable chemical reagent, surface features like arrangement and size of grains, the distribution of phases, the results of plastic deformation and the existence of impurities and flaws can be revealed. In this study the author was interested in measuring the coating thickness and also viewing the phase distribution in the coating surface and cross-section.

The light microscope consists essentially of three parts: (i) an illuminator, to illuminate the surface of the metal, (ii) an objective, and (iii) an eyepiece, to form and enlarge the image. Figure 5.1 illustrates the principle of the metallurgical compound microscope and final virtual image formation. A light microscope reveals no fine-scale atomic details, such as the structure of a crystal or the existence of dislocations, because of the limited resolving power. The smallest distance, δ, that may be resolved is controlled by three factors, (i) the wavelength of the illumination, λ, (ii) the effective aperture of the objective lens, and (iii) the medium between the lens and the specimen, according to the relation,

$$\delta = \frac{0.5\lambda}{Numericalaperture} = \frac{\lambda}{2\mu\sin\alpha} \tag{5.3}$$

Therefore, the resolution of an optical microscope increases with increase in numerical aperture, that is by increasing the refractive index of the medium and the half angle α subtended by the maximum cone of rays entering the objective. However, even in the most favorable case with α approaching 90°, the resolution cannot exceed 200 nm, because the wavelength of light is about 500 nm. The maximum magnification obtained with the optical microscope is about 2,000X.

The greatest advance in resolving power was obtained by the electron microscope. High-velocity electrons behave like very short wavelength radiation. The electron beams in electron microscopes are associated with a wavelength nearly 100,000 times smaller than the wavelength of visible light, thus greatly increasing the potential resolving power. One of the methods of electron microscopy is discussed in next section.

5.3.2 Scanning Electron Microscopy

Scanning electron microscopy is the most widely used technique to characterize very small features of surfaces with a micrometer or even less resolution. In this technique, the area to be examined or the microvolume to be analyzed is irradiated with a finely focused electron beam. A schematic of a combination instrument, which can be operated as an electron microprobe and as a SEM, is shown in Figure 5.2. Electrons thermionically emitted from a tungsten or lanthanum hexaboride (LaB_6) cathode filament are drawn to an anode, focused by two successive condenser lenses into a beam with a very fine spot size (~ 50 Å). Pairs of scanning coils located at the objective lens deflect the beam either linearly or in raster fashion over a rectangular area of the specimen surface. Electrons having energies ranging from a few KeV to 50 KeV, with 30 KeV a common value, are utilized. Upon impinging on the specimen, the primary electrons are scattered elastically and some lose energy to other atomic electrons and to the lattice, inelastically. The types of signals produced when the electron beam impinges on a specimen surface include secondary electrons, backscattered electrons, Auger electrons, characteristic X-rays, and photons of various energies. These signals are obtained from specific emission volumes within the sample and can be used to examine many characteristics of the sample (surface topography, composition, crystallography, etc.) [18,28].

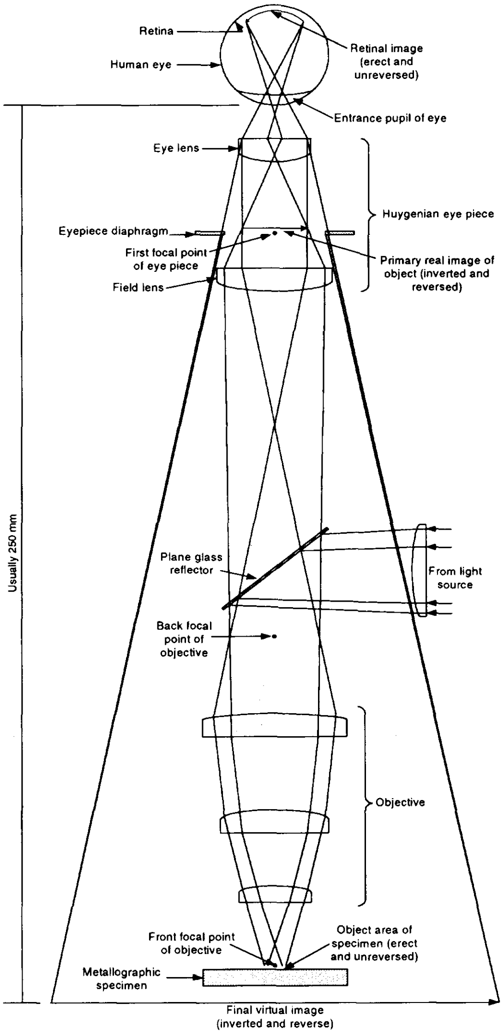

Figure 5.1 Schematic of a metallurgical microscope and image formation [29].

In the scanning electron microscope (SEM), the signals of greatest interest are the secondary and backscattered electrons, since these vary according to differences in surface topography as the electron beam seeps across the specimen. The secondary-electron emission is confined to a volume near the beam's impact area, permitting images to be obtained at relatively high resolution. Other signals are available, which prove similarly useful in many cases.

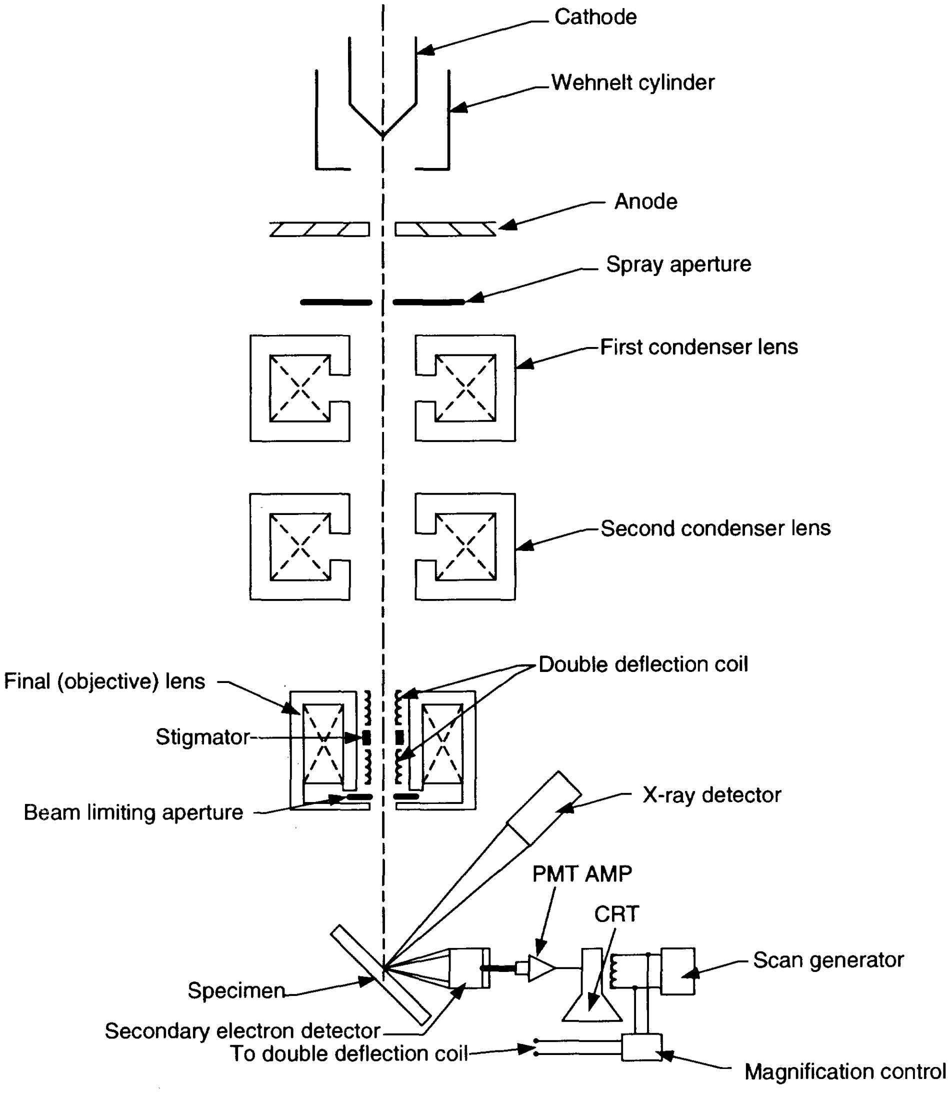

Figure 5.2 Schematic of a scanning electron microscope [28].

In the X-ray Energy Dispersive analysis (EDX), frequently referred to as the electron microprobe, the primary radiation of interest is the characteristic X-rays emitted as a result of the electron bombardment. The analysis of the characteristic X-ray can yield both qualitative identification and quantitative compositional information from region of a specimen as small as a micrometer in diameter.

5.4 Nuclear Reaction Analysis

Nuclear reaction analysis is one of the techniques used in Ion Beam Analysis (IBA). IBA utilizes high-energy ion beams to probe elemental composition non-destructively as a function of depth to several microns with a typical depth resolution of 100-200 Å. It is a fast and non-destructive technique and no standards are required to quantify the absolute atomic ratios in compounds or mixtures, insensitive to their chemical environments. It can also determine the film thickness (or density) as well as the structural disorders in single crystalline targets. Energy distribution of backscattering ions quantifies the depth distribution for a given element. Distinctive characteristic X-rays emitted from the different target elements upon the beam bombardment ensure the accurate identification of similar mass elements. Gamma rays emitted from the beam-induced nuclear reactions provide an excellent sensitivity (~ ppm) and/or depth resolution (~ 50 Å) for certain light isotopes such as ^{1}H, ^{15}N, and ^{19}F [30]. IBA is a broad term that involves several specific techniques, mainly:

- Rutherford backscattering spectrometry (RBS)
- Nuclear reaction analysis (NRA)
- Forward recoil spectrometry (FReS) or elastic recoil detection analysis (ERDA)

- Particle induced X-ray emission (PIXE) analysis
- Ion channeling analysis

NRA technique was used for tantalum and tantalum nitride films characterization and is discussed here. Microanalysis by nuclear reaction analysis uses low range nuclear forces. When a charged particle moving at high speed strikes a material, it interacts with the electrons and nuclei of the material atoms, forming a compound nucleus in a highly excited state that disintegrates by the emission of gamma ray in a small time. The energy of gamma radiation is characteristic of the elements, which take part in the nuclear reaction. The products of the reaction are charged particles, gamma ray or both, that is,

$$a + Y \rightarrow b + Z + n\gamma \tag{5.4}$$

where, a = incident particle nucleus

Y = target nucleus

b = emitted particle

Z = residual nucleus

$n\gamma$ = probability of a cascade of n gamma rays

Advantages

- Non-destructively measures light elemental depth profiles ($Z<9$) with a superb sensitivity of a few ppm, a good depth resolution of a few nanometers, and a maximum depth of a few microns. Elements like H, N, Li, B, C, O, and F can be analyzed.

- Unlike ion scattering techniques, NRA is an isotopically sensitive technique with an excellent mass resolution and has no mass-depth ambiguity of RBS in data interpretation.
- Channeling-NRA can be used to determine lattice location of impurities and defect distribution depth profile in single crystalline samples.

Limitations

- For the nuclear reaction to happen, the repulsive Coulomb barrier has to be surmounted. For light particles (proton, deuteron, helium3 and 4) of energy up to 3 MeV, the only accessible elements are the light elements with $Z<15$.
- Unlike RBS, NRA method does not have continuous sensitivity, because detection of an element depends on whether reaction has or has not occurred in the cross-section being analyzed.

CHAPTER 6

ADHESION TEST FOR THE COATINGS

For a coating to be a good protection barrier, it has not only to be continuous and with as few defects as possible, but also, strongly adhering to the substrate it intends to protect. Thus, the usefulness of thin coatings can be limited by its adhesion to the substrate. One of the simplest ways to measure adhesion is to apply an adhesive tape to the surface of the coating or the film, and to subsequently examine the result of stripping. Those, which are weakly bonded to the substrate, will come off easily while those, which are strongly bonded, will remain on the substrate. However, the above method is highly qualitative and gives no indication of the relative magnitudes of adhesive forces. The major experimental hurdle encountered in the thin coatings is often making a mechanical linkage to the coating so as to be able to strip it off. A specific test, namely the scratch test that is considered here, circumvents this linkage problem.

6.1 Principles of Scratch Test

Essentially, the test consists in deforming the coating-substrate interface by straining the substrate. The mechanical resistance of the interface and/or of the coating is characterized by a critical load, which is the minimum load at which damage by separation of the coating from the substrate can be observed. More specifically, a spherically tipped stylus with a given load or a gradually increasing load is drawn across the sample under test. The load is increased with each traverse to give a series of scratches or the load is increased gradually at a fixed rate in a single scratch until the coating is stripped cleanly from the scratch channel. The stylus is thought to produce a shear force at the coating-substrate interface around the rim of the indentation so that the critical load at which the coating is stripped off can be taken as a measure of the adhesion [31-33].

6.2 Scratch Tester

A commercially available scratch tester, Revetest Automatic Scratch Tester developed by Centre Suisse d'Electronique et de Microtechnique (CSEM), fitted with a Rockwell C diamond (conical angle, 120°; hemispherical tip of 200 μm radius) tip was used for our studies. The applied load could either be kept constant or linearly increased while scratching. This tester was equipped with an integrated optical microscope (Figure 6.1), an acoustic emission detection system (with a transducer mounted just above the diamond stylus) and a device to measure the tangential frictional force (in the scratching direction), giving the friction coefficient value during scratching. The critical load for a coating-substrate system can be determined by optical, acoustical or mechanical methods. When series of similar samples have to be tested for their critical load, the main criteria to be used are, first acoustic emission and second the frictional force; these two criteria, however do not replace the optical observation which in addition gives useful indications on the size and nature of the failures. In most cases, it can be said that the three methods provide complementary information.

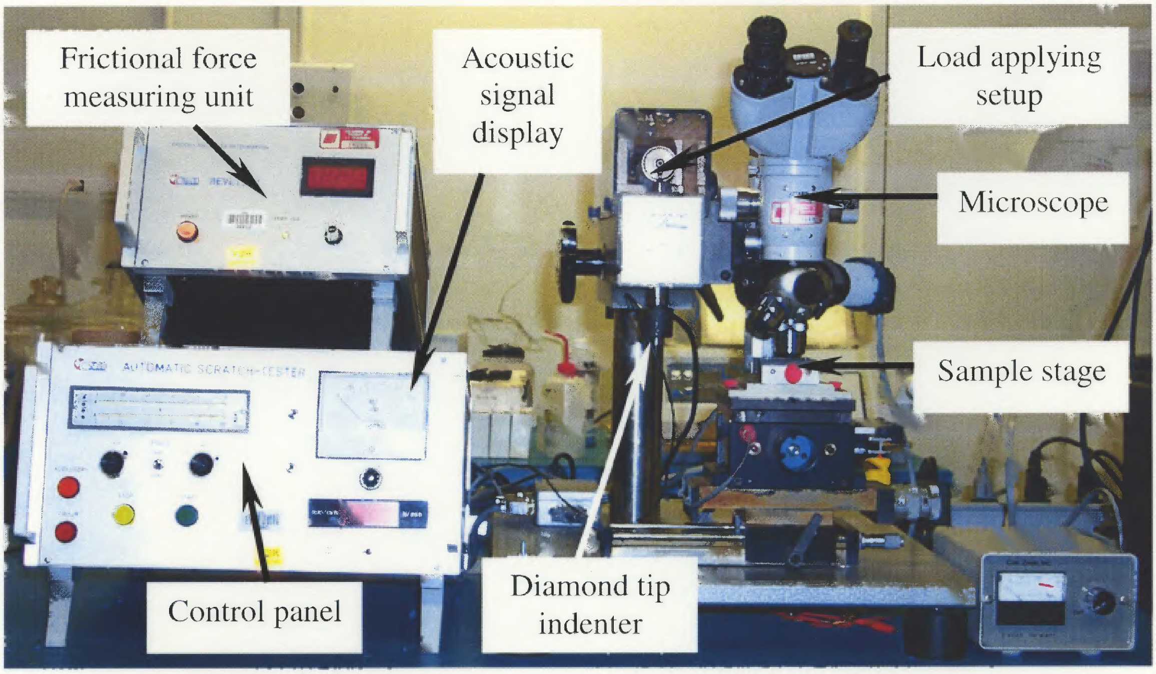

Figure 6.1 Revetest Automatic Scratch Tester.

Two distinct types of metal coating failure generally occur. Brittle coatings tend to crack and partially detach owing to the failure of the coating and of the coating-substrate interface to support the degree of deformation. The cracking is then following by spalling of the coatings, part of which can be pressed into the substrate again, so that loss of adhesion is not necessarily accompanied by a complete physical removal of the coating from the channel by the stylus. In contrast, soft coatings tend to form a hillock ahead of the stylus and to leave folds at the edge of the channel without necessarily becoming detached. The coating can also be extruded sideways under the stylus and thinned to transparency so that it appears as though the coating has been removed, although loss of adhesion has not occurred. In spite of the varied behavior, which can be encountered in the scratch test, the test could be used quantitatively to compare the adhesion of similar films on identical substrates [31,32].

6.3 Influence of Parameters on Critical Load

Before analyzing the results from a scratch test, it is necessary to consider the influence of the intrinsic parameters (related to the scratch tester) and the extrinsic parameters (related to the coating system being tested). Since no literature on adhesion testing of tantalum coatings on steel was available, our results and discussion about this system have been based on studies by Steinmann et al [33], who used TiC-, Ti(C,N)- or TiN-coated steels or cemented carbides, deposited by CVD and PVD. The conclusions of this study, as discussed below are found to be good enough for our samples too.

6.3.1 Intrinsic Parameters

6.3.1.1 Loading Rate and Scratching Speed. The critical load is independent of the loading rate (dL/dt) and scratching speed (dx/dt), provided that their variations are proportional, that is, the ratio dL/dx remains constant. Consequently, the dL/dx ratio is a significant parameter for the scratch test. The critical load decreases when the dL/dx ratio decreases; the differential critical load variations become more important for the lower dL/dx values. This behavior is explained by the fact that, when dL/dx decreases, the probability of encountering defective adhesion of the coating within a certain load range increases: this consequently results in a decreased critical load. Therefore, when the loading rate is kept constant, the critical load decreases when the scratching speed increases; when the scratching speed remains constant, the critical load increases when the loading rate increases.

6.3.1.2 Indenter Tip Radius. The average pressure P_m applied by the spherical point and related to the plastic deformation of the substrate at the moment the critical load is reached is an approximation of the substrate hardness, $P_m \approx H = 2L_c/\pi b^2$ where b is half-width of the scratch. Because b is proportional to the indenter tip radius R, above expression shows that the critical load must be proportional to R^2. However the experimental results show that critical load varies with $R^{0.85}$ to $R^{1.10}$, depending on the value of dL/dx.

Since the critical load depends on the loading rate, the scratching speed and the indenter tip radius, it is necessary to define standard operating conditions in order to minimize the number of parameters influencing the critical load. The recommended standard operating conditions by the manufacturer are as follows:

dL/dx = 10 N/mm

R = 200 μm

These two values result from a compromise. If the load increase per unit length is too large the resulting critical load will be lacking resolution. However, when the dL/dx ratio is smaller than 10 N/mm, the resulting critical load is too sensitive to small variations of this dL/dx ratio. To assure sufficient deformation of the substrate, the tip radius R should be chosen as large as possible with respect to the coating thickness; however, R is limited by the loading capacity of the instrument. On the whole a tip radius of 200 μm suits most coatings and is convenient since this corresponds to the geometry used for the Rockwell C hardness test and is therefore readily available.

6.3.1.3 Diamond Tip Wear. The critical load does not vary much with the number of scratches performed, until noticeable tip damage has occurred. The critical load values vary from one diamond to another, which may be due to variation in the chemical composition of the diamond with respect to the inclusions and surface impurities, the surface quality and the initially present micro cracks. Diamond wear is of course a function of the hardness of the scratched sample, and increases with the hardness of both the coating and the substrate. The critical load values are influenced once the diamond tip has undergone noticeable damage and these values no longer reflect the adherence of the tested system. The lifetime of a diamond can be extended through regular microscopic observations, since the diamond can be rotated through 180° before catastrophic damage is reached.

6.3.2 Extrinsic Parameters

6.3.2.1 Substrate Hardness and Coating Thickness. The extent of the coating-substrate assembly deformation caused by the scratching point is mainly dictated by the substrate deformation. When the substrate hardness is increased, there is need for a higher load to obtain the same plastic deformation. Assuming the adhesion to be the same, the critical load being a function of the degree of deformation, increases with the substrate hardness. Similarly, coating thickness increase requires an increased load to obtain the same degree of deformation and therefore the critical load increases with the coating thickness.

6.3.2.2 Coating Roughness. Coating roughness (> 0.3 μm) due to surface defects like peaks, holes and whiskers complicate the microscopic observation to determine critical load. The actual critical load resulting from adhesive failures may be hard to measure due to high coating roughness.

6.3.2.3 Substrate Roughness Prior to Coating. The critical load values go up as the substrate roughness prior to coating decreases. Hence, it is generally believed that adhesion of films and coatings is improved with increase in degree of polishing of the substrate.

6.3.2.4 Frictional Force and Coefficient of Friction. Along with all the above-mentioned extrinsic factors affecting adhesion, the critical load and the tangential frictional force also depend on the friction coefficient between the indenter and the coating surface; higher values for the coefficient of friction correspond to lower critical load values. One of the three criteria (mentioned previously) used to determine the critical load is the tangential frictional force (used to calculate coefficient of friction). The critical load determined by the frictional force is that load at which a sudden change in frictional force occurs. The data obtained from the frictional force cannot be considered singly to determine critical load, but is complementary to the acoustic emission signal and the optical microscopy observation.

The results from adhesion testing of the tantalum coatings are discussed in Chapter 7.

CHAPTER 7

RESULTS AND DISCUSSION

The main aim of this work was to study the sputtering process parameters and substrate surface preparation requirements, yielding 100 % α-phase in the deposited tantalum coatings. Deposition was carried out on more than 300 steel substrate samples, of which about 40 samples had tantalum deposited on bare steel at room temperature, about 80 samples were prepared by tantalum deposition on heated substrates and remaining samples had a nitrided tantalum interlayer deposited on steel substrate, prior to subsequent tantalum deposition, at room temperature. In every experiment, silicon and oxidized silicon control substrates were mounted on each substrate holder, for thickness and resistivity measurement. The deposition conditions used during sputtering for all the samples discussed in this chapter are tabulated in Appendix B.

7.1 Thickness Measurement

The thickness of films and coatings was measured using Sloan Dektak IIA stylus profilometer (refer to Section 5.1) on Si and SiO_2 control substrates. Steel substrates, due to higher surface roughness, did not give straight-line profiles, which made reliable thickness measurement difficult. Hence, thickness was not measured on them; rather an estimate of thickness on steel was made from the thickness measurements on Si and SiO_2 substrates. Figure 7.1 shows typical profile readout from the profilometer. In this case, the step in the profile corresponds to a thickness of 4.7 μm of Ta on oxidized silicon substrate (sample 022502-PTa02c). A step was formed on the substrate by masking a part of it by a small piece of steel foil. The minimum thickness, which this profilometer can reliably measure, was 0.1 μm, but tantalum coating thicknesses deposited for this study were in the range of 0.3-60 μm.

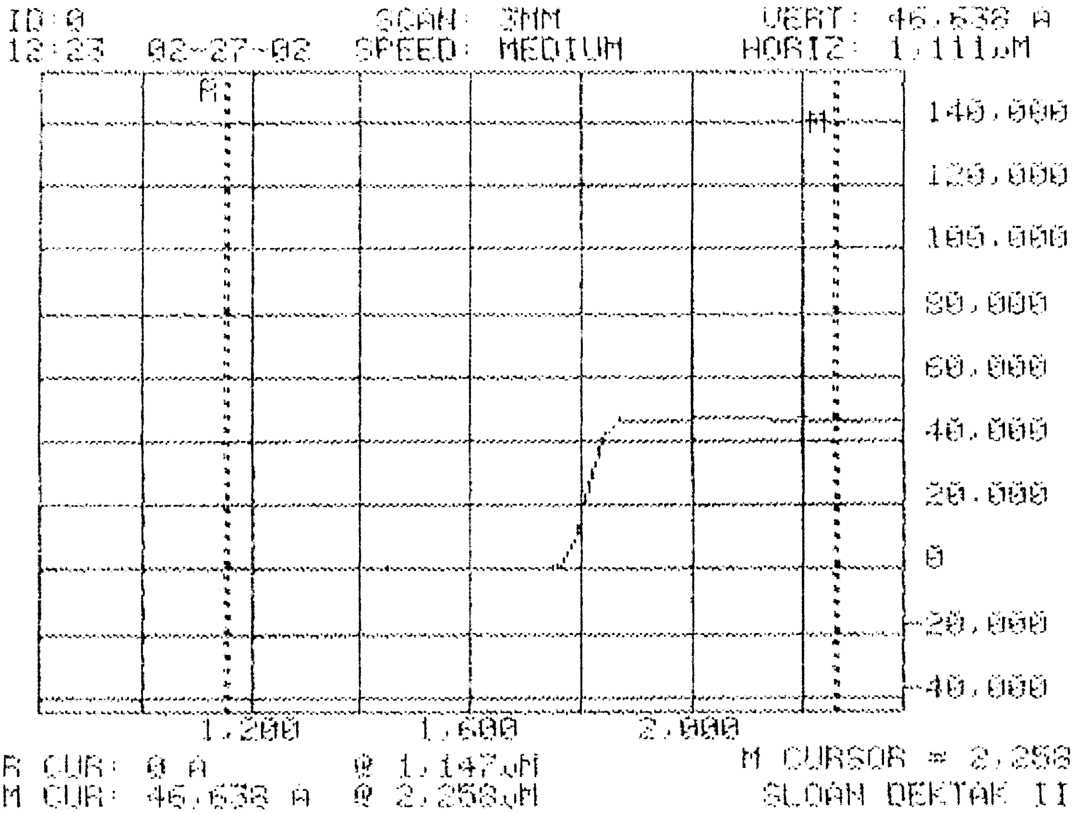

Figure 7.1 Dektak profile for tantalum coating deposited on oxidized silicon substrate – film thickness 4.7 μm.

For thick coatings (> 25 μm), the thickness was measured using an optical microscope, from the sample cross-section, after the sample was cut into two pieces at the center by a diamond saw. Figure 7.2 illustrates an example of thickness measurement by optical microscopy. Coating was deposited at 1 mtorr pressure of Ar gas at 0.5 A current for 8 hours (sample 021102-PTa01a3). The estimated coating thickness of this sample was 46 μm.

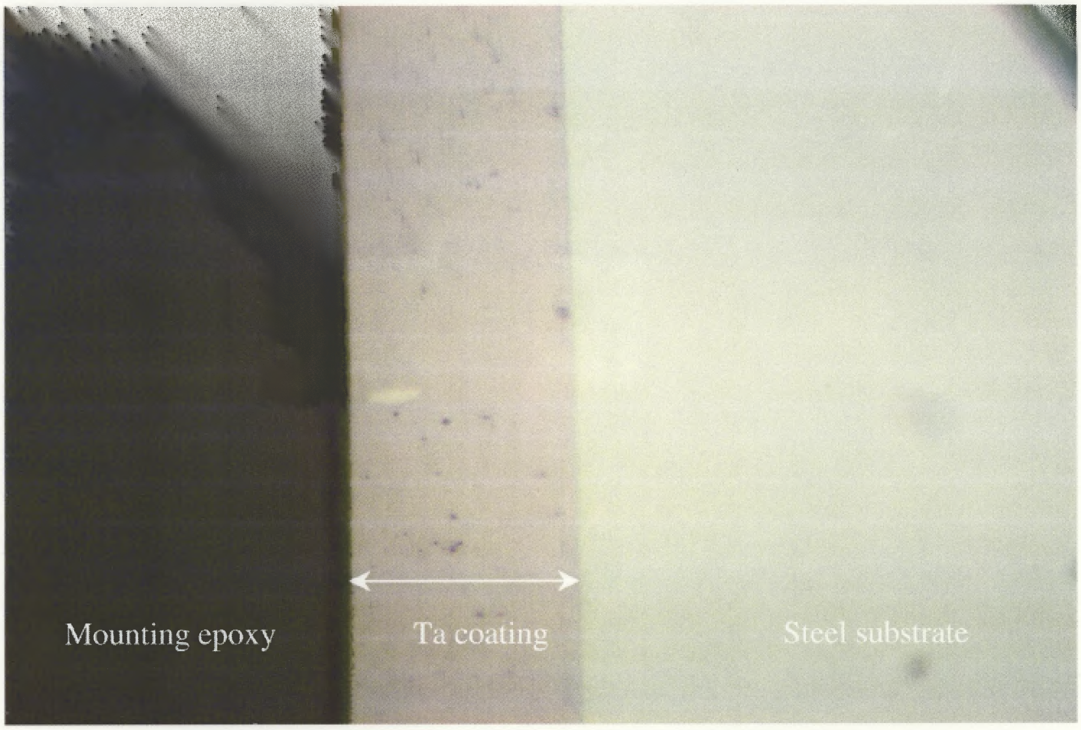

Figure 7.2 Cross-sectional view of the tantalum coating on steel substrate seen under an optical microscope - coating thickness 46 μm (sample 021102-PTa01a3).

7.2 Influence of Deposition Conditions on Phase of Tantalum

To determine phases present in the coatings, x-ray diffraction analysis was done. Philips X'Pert x-ray diffractometer, using Cu-K_α radiation, was employed for x-ray diffraction studies (see Section 5.3). The indexing of x-ray diffraction patterns was done by comparing the measured spectra with the standard powder diffraction data for bcc (alpha) tantalum (JCPDS Ref. Card No. 04-788) and beta tantalum (JCPDS Ref. Card No. 25-1280). The standard powder diffraction spectra for bcc tantalum and tetragonal β-tantalum are shown in Appendix A. This x-ray diffractometer can only identify the phases in approximately 1 μm layer of tantalum at the surface because of the absorption of x-rays diffracted from the material below this thickness. Phase distribution in thick coatings was observed using the metallographic technique, based on different optical reflectivity of the two tantalum phases.

Three different methods were used to deposit tantalum on steel substrates, viz., tantalum coating deposition on bare steel substrate at room temperature with argon and krypton sputtering gases, tantalum deposition on bare steel substrates heated to elevated temperatures, with Ar and Kr as sputtering gases, and, tantalum deposition on nitrided tantalum interlayer deposited on steel substrate prior to tantalum coating. In the last method of deposition, the nitride interlayer and tantalum was deposited at room temperature with Ar as the working gas. The process parameters involved in the experiments are listed in Appendix B.

7.2.1 Tantalum Coatings on Bare Steel Substrates at Room Temperature

Figure 7.3 shows the XRD spectrum of 8 μm thick tantalum coating deposited on bare steel at room temperature in argon atmosphere. Peaks are labeled by crystallographic planes corresponding to the two tantalum phases, based on comparison with the standard spectra. Mixed phase (alpha as well as beta-phase) was observed in this sample (082401-PTa02a). Figure 7.4 is the XRD pattern of 8 μm thick tantalum coating deposited on bare steel at room temperature in krypton atmosphere. In this sample (081601-PTa01a), only beta was found with no trace of alpha phase.

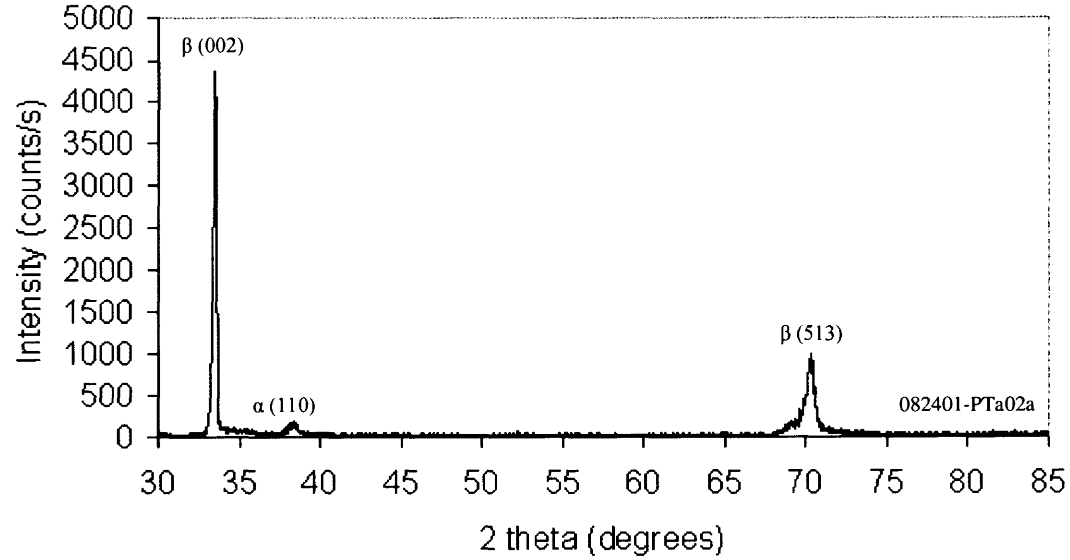

Figure 7.3 XRD spectrum of tantalum coating sputter-deposited on steel substrate at room temperature with Ar sputtering gas.

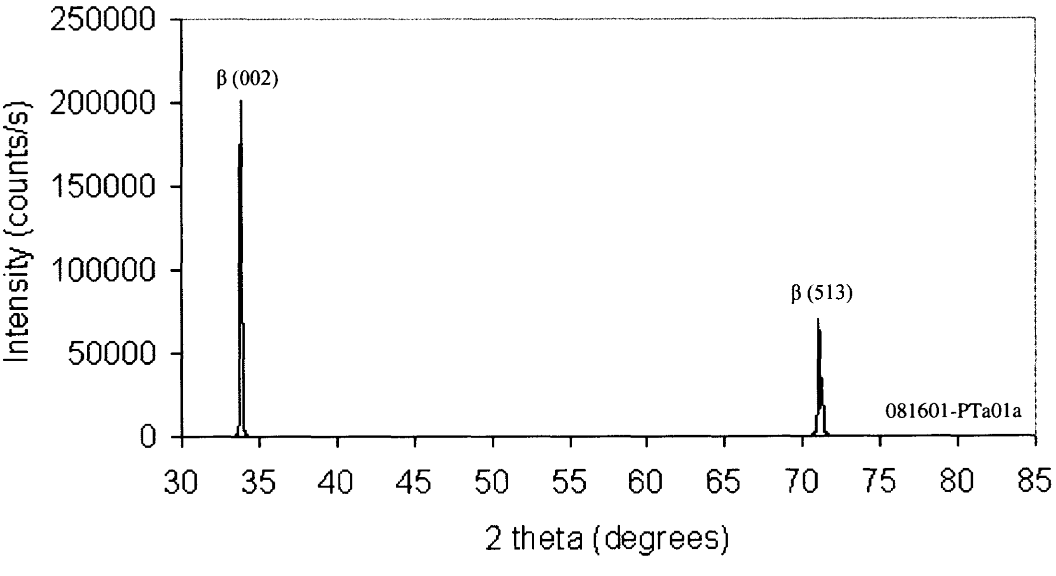

Figure 7.4 XRD spectrum of tantalum coating deposited on steel substrate at room temperature with Kr sputtering gas.

7.2.2 Tantalum Coatings on Heated Substrates

Tantalum coatings were deposited on heated steel substrates at elevated temperatures, using Ar and Kr sputtering gas. Initially, it was found that above a threshold temperature (300°C for argon sputtering gas and 250°C for krypton sputtering gas), pure bcc-phase could be grown in the coatings. Figure 7.5 show two XRD patterns from different coating samples with different deposition conditions. Sample 082401-PTa05a was deposited with Ar sputtering gas on steel substrate heated to 300°C; whereas sample 081601-PTa03a was deposited on steel substrate heated to 250°C with Kr as sputtering gas. Both coating samples consisted of pure alpha phase. High intensity of peak at 38.5° indicated that (110) plane was a preferred orientation of the alpha phase growth. In recent experiments, the temperature was measured more accurately using a thermocouple with a better thermal contact to the substrate holder. Precise threshold temperature still needs to be determined, but based on the recent data, the threshold temperature (T_t) can be set at $350°C < T_{t,Ar} \leq 400°C$, for argon sputtering gas, and for krypton sputtering gas, $T_{t,Kr}$ should be 50°C lower than $T_{t,Ar}$. Mixed phase was grown in coatings deposited on under-heated steel substrates. This is illustrated in the XRD spectra in figure 7.6.

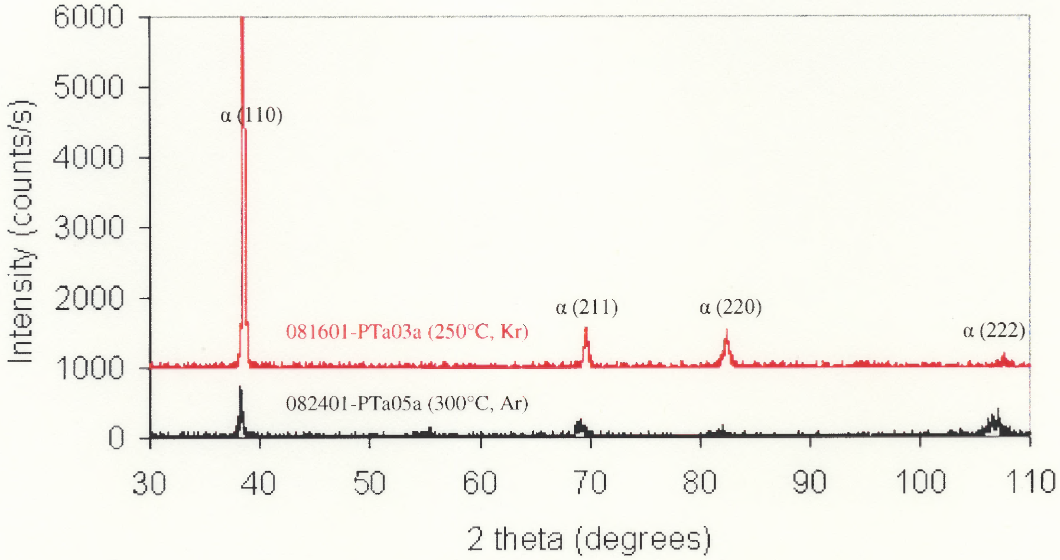

Figure 7.5 XRD patterns of two coating samples produced on steel substrate heated to 300°C and 250°C with Ar and Kr sputtering gas respectively.

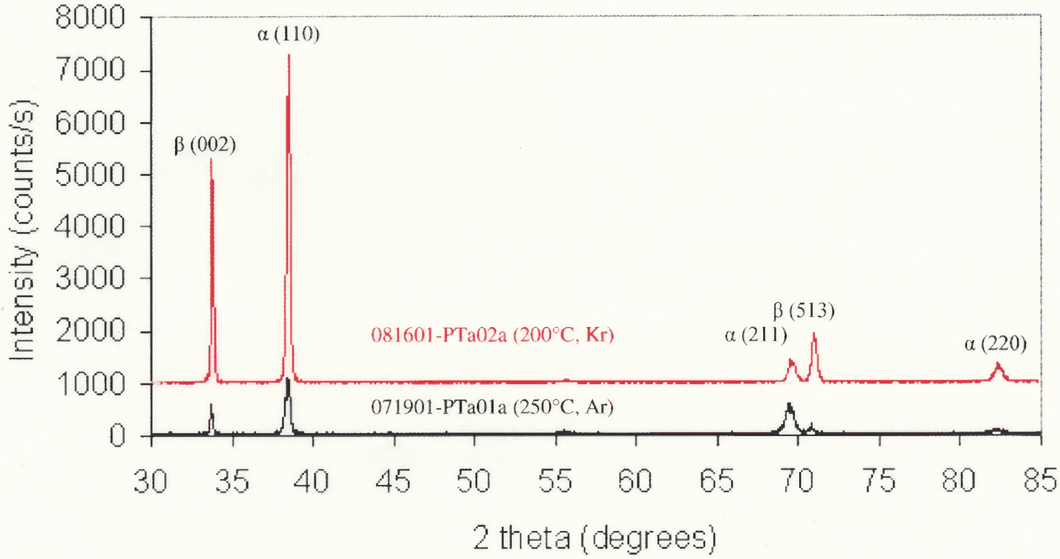

Figure 7.6 XRD patterns of tantalum coatings deposited on under-heated (below the threshold temperatures) steel substrates with Ar and Kr sputtering gases.

7.2.3 Tantalum Coatings on Steel Substrates with Nitrided Tantalum Interlayer between Substrate and Coating

A set of experiments was performed, in which, tantalum coatings were deposited (with argon sputtering gas) on steel substrate with a nitrided tantalum interlayer. In-situ sputter etching (refer to Section 4.2) exposes a cleaner surface for films to deposit [36]. Hence a series of sample coatings were produced on steel substrates, which were sputter etched prior to deposition of nitride interlayer and then tantalum coating on it. The sputter etching was performed in argon plasma, with Ar flowing at 18 sccm through the chamber and pressure ranging from 180 mtorr to 240 mtorr. The discussion of the results is divided into two parts depending on whether sputter etching was performed or not.

Not Sputter Etched Steel Substrates

The nitride interlayer was deposited by reactive sputtering with a mixture of nitrogen and argon gases, prior to tantalum deposition. The flow rate of the working gases was varied from 1-9 sccm (for N_2) and 3-18 sccm (for Ar). Most of the depositions were performed with argon flow rate of 18 sccm, which resulted in a stable source operation. The flow rates of the sputtering gases were expressed as a ratio, for example, 2/18, where, numerator is the value of flow rate of nitrogen gas (in sccm) and denominator is the argon gas flow rate (in sccm). Due to the limitation of the profilometer, unable to measure thickness less than 0.1 μm, the thickness of nitride interlayer was estimated from the deposition rate calculated from thickness measured on thick nitride coatings deposited under similar process conditions. The interlayers of various thicknesses, ranging from 5 nm to 1 μm, were deposited with various flow rates. It was found that a nitride interlayer with a minimum thickness of 20 nm deposited at flow rates of 2/18, 3/18, 4/18, 5/18 and

7/18 yielded pure bcc-tantalum in the final coatings. Thickness less than 20 nm in case of 2/18 working gas rates did not always produce pure bcc-phase in the tantalum coatings. Also, flow rates of 1/18 and 1/6 were tried, but tantalum grown on such interlayers had mixed phases. Figure 7.7 show XRD patterns of some selected coating samples deposited on a steel substrate at room temperature with a nitride interlayer. The flow rates of N_2/Ar used for the nitride interlayer in samples 020502-PTa02a and 020502-PTa03a were 2/18 and 3/18 respectively. The estimated interlayer thickness was 20 nm in both samples. The XRD spectra revealed only alpha peaks, with no trace of beta peaks in it.

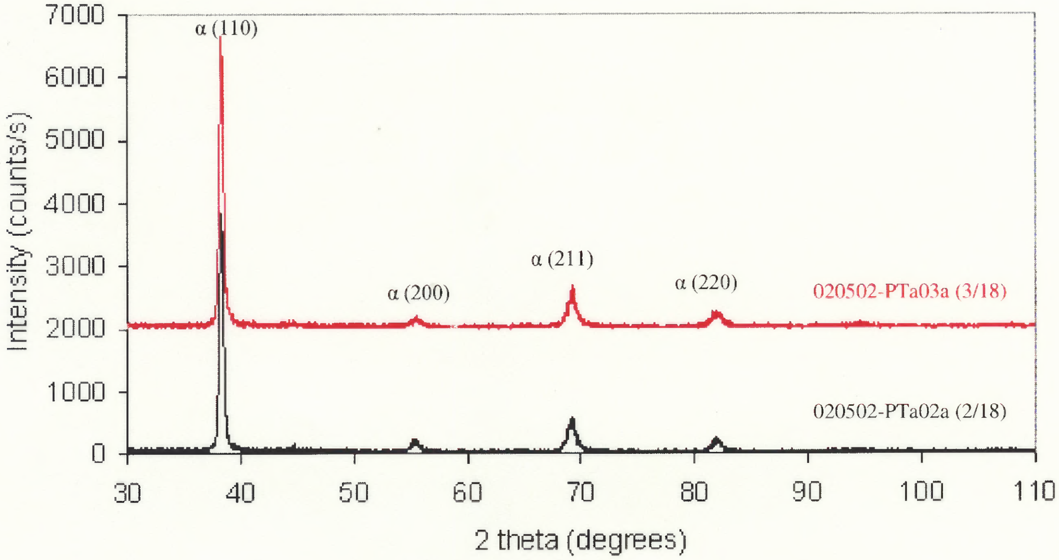

Figure 7.7 XRD patterns of coating samples deposited on nitrided tantalum interlayer on steel substrate at room temperature. Nitride interlayers (~20 nm thick) were deposited at pressure of 5 mtorr, with 2/18 and 3/18 N_2/Ar flow rate ratios.

To determine the stoichiometry of the nitride formed in the interlayer, thicker (~ 1 μm) nitride films were deposited on steel substrate using similar deposition conditions to facilitate comparison. These films were then subjected to x-ray diffraction.

The measured x-ray diffraction patterns from the deposited nitride films were then compared with the standard peaks of various crystallographic structures formed by tantalum and nitrogen compounds [34]. Figure 7.8 shows the XRD spectra of nitrided tantalum films deposited at various N_2/Ar flow rate ratios. Two peaks of stoichiometric tantalum nitride were observed in the spectra of samples deposited with 2/18, 3/18, 4/18, and 5/18 flow rates. The peak at 35.7° corresponds to fcc (111) TaN, while the peak at 41.1° is related to (200) TaN. In nitride deposited with 1/30 flow rates, peaks at 35.9° and 38.5° were observed, which could be ascribed to (002) and (101) of Ta_2N respectively [34]. It was suggested that cubic TaN phase facilitated epitaxial growth of alpha phase tantalum on top of it, due to similar crystal structure. Mixed phase tantalum coating observed on nitride interlayer corresponding to 1/30 flow rates can be explained by the presence of hexagonal Ta_2N in it, which does not help in epitaxial growth of alpha phase.

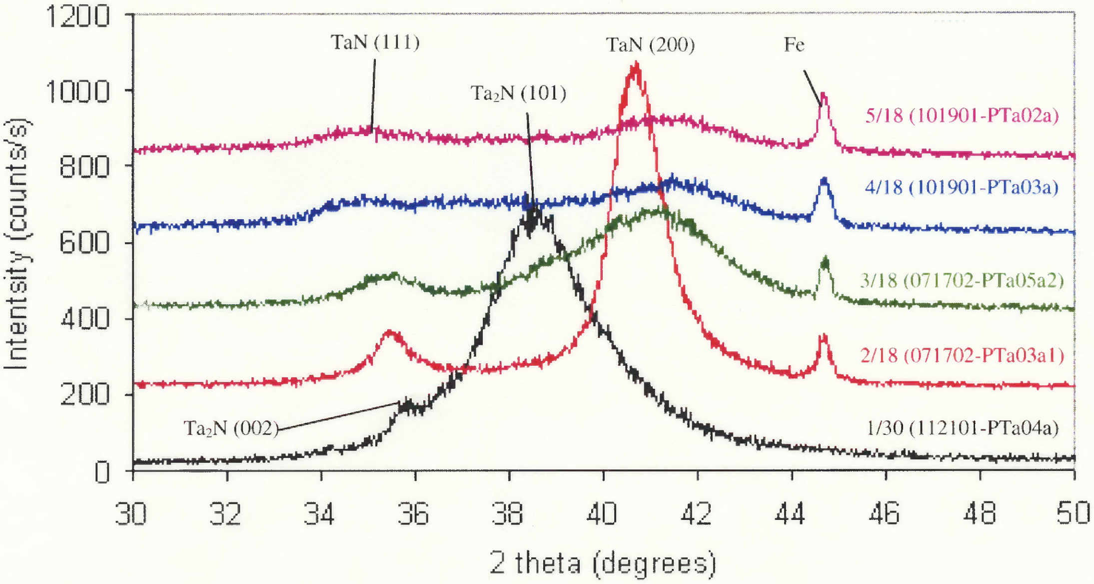

Figure 7.8 XRD patterns of nitride interlayers deposited on steel substrate with various nitrogen and argon gas flow rates.

The atomic percentage of nitrogen in some nitrided tantalum samples was obtained, using nuclear reaction analysis technique (refer to Section 5.5.2). The results obtained from this analysis are shown in Figure 7.9. The energy of proton beam was increased in small steps, so that the intensity of the detected γ-radiation from $^{15}N(p,\alpha\gamma)^{12}C$ nuclear reaction was proportional to the nitrogen concentration at a depth where the protons passing through the sample were slowed down to the resonance energy. Two samples of 1 μm and 0.8 μm thick nitrided tantalum films, deposited on steel substrate with nitrogen and argon flow rates of 1/18 and 3/18 respectively, at a pressure of 5 mtorr, were subjected to NRA. The absolute nitrogen concentration could be measured with an appropriate calibration standard, while the distance of the probed volume from the surface of the sample was estimated from TRIM simulations [35]. The results of NRA show approximately 50 at. % nitrogen content in the nitride film deposited at 3/18 flow rates, which confirms stoichiometric TaN composition. In nitride film deposited at 1/18 flow rates, only 30 at. % nitrogen was found, which indicates Ta_2N stoichiometry in the film.

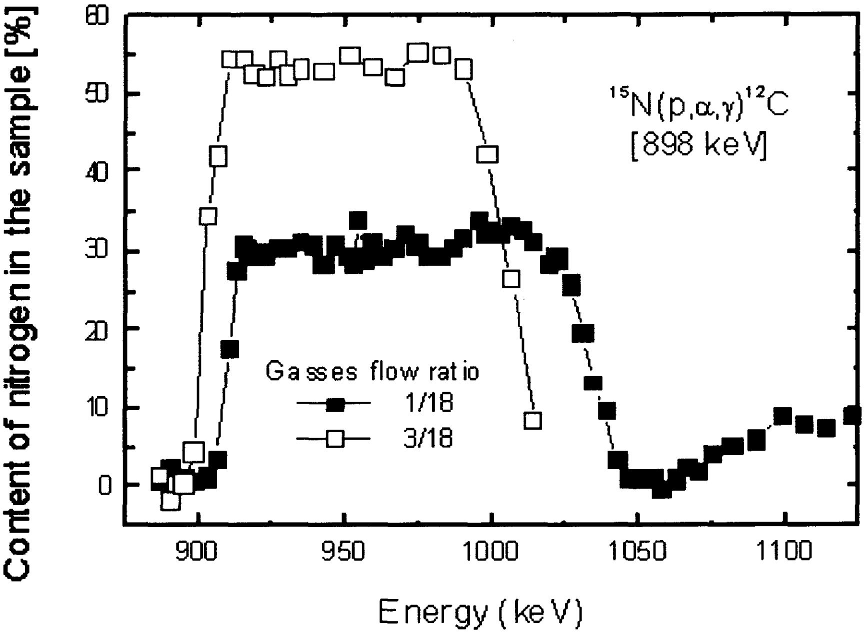

Figure 7.9 Nuclear reaction analysis to determine the nitrogen content in tantalum nitride tantalum films deposited at nitrogen and argon flow rates of 1/18 and 3/18.

Sputter Etched Steel Substrates

Figure 7.10 shows the XRD patterns of tantalum coatings deposited under similar conditions, with nitrided tantalum interlayer, on sputter-etched and not sputter-etched substrates. The interlayer thickness was ~20 nm in both samples and the nitride deposition was done with N_2/Ar flow rates of 2/18 sccm. Sample 021102-PTa01a2 was sputter-etched with argon sputtering gas at 220 mtorr pressure and 18 sccm flow rate for 20 minutes. The peaks observed in sample 021902-PTa01a4 corresponded to alpha phase with no trace of beta phase. In sputter etched substrate sample, the peaks at 33.6° and 71.0° corresponded to diffraction planes (002) and (513) of beta phase along with other alpha peaks.

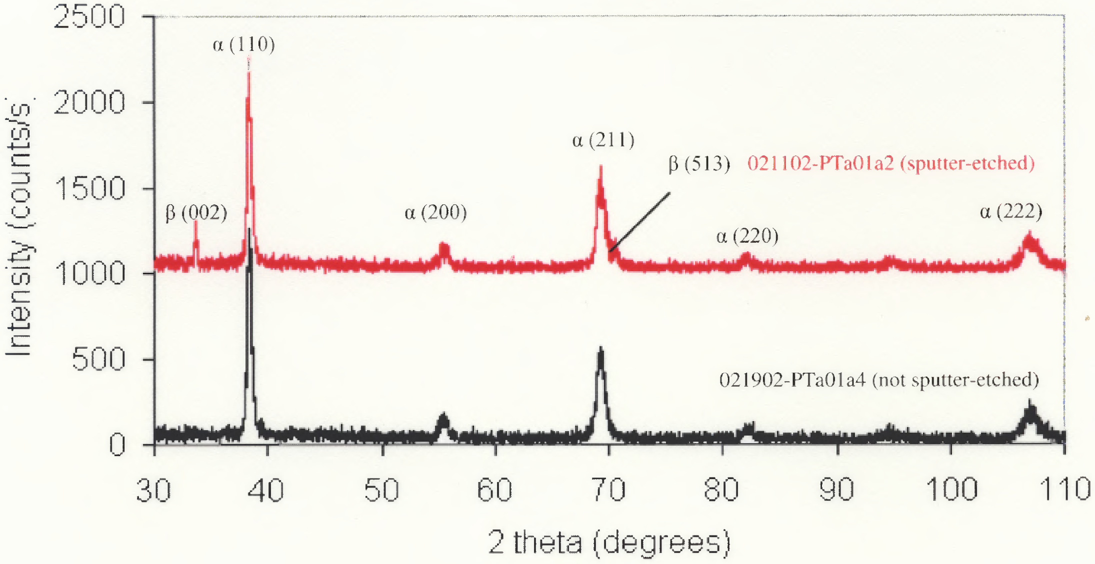

Figure7.10 XRD patterns of tantalum coatings deposited under similar conditions, on nitride interlayer, on not sputter etched and sputter etched steel substrates.

It was suspected that, sputter etching of steel substrate might affect the structure of deposited tantalum nitride. Figure 7.11 shows the XRD patterns of tantalum nitride deposited on sputter-etched and not sputter-etched steel substrates. Patterns of tantalum nitride grown with two different flow rates of N_2/Ar, viz., 2/18 and 3/18 are shown in this graph. The positions of the intense diffraction peaks did not vary, suggesting no change in structure of TaN formed due to sputter etching. The intensity of (200) peak, however, decreased for sputter-etched sample (071702-PTa04a) as compared to not sputter-etched sample (071702-PTa03a), deposited under 2/18 flow rate conditions. On the other hand, the films deposited with 3/18 flow rates do not show any substantial difference in intensities of same peaks. Hence it was concluded that sputter etching did not have an effect on the structure and orientation of tantalum nitride deposited at a flow rate ratio of 3/18. At the flow rate ratio of 2/18, although the structure of the films with and without sputter etching was the same, the film orientation appears to be different, as indicated by the change in the relative intensities of the peaks. This change of orientation is probably responsible for the difference in the phase composition of tantalum films, shown in Figure 7.10. In case of sputter etched substrates, although, the diffraction peaks observed in the sample (corresponding to 2/18 flow rate ratio) were related to TaN stoichiometry of the interlayer, the phase composition of the tantalum coatings deposited over the nitride interlayers was not consistently bcc-phase. This suggests that formation of tantalum nitride in the interlayer is a necessary condition but not sufficient condition required for obtaining alpha phase tantalum coatings.

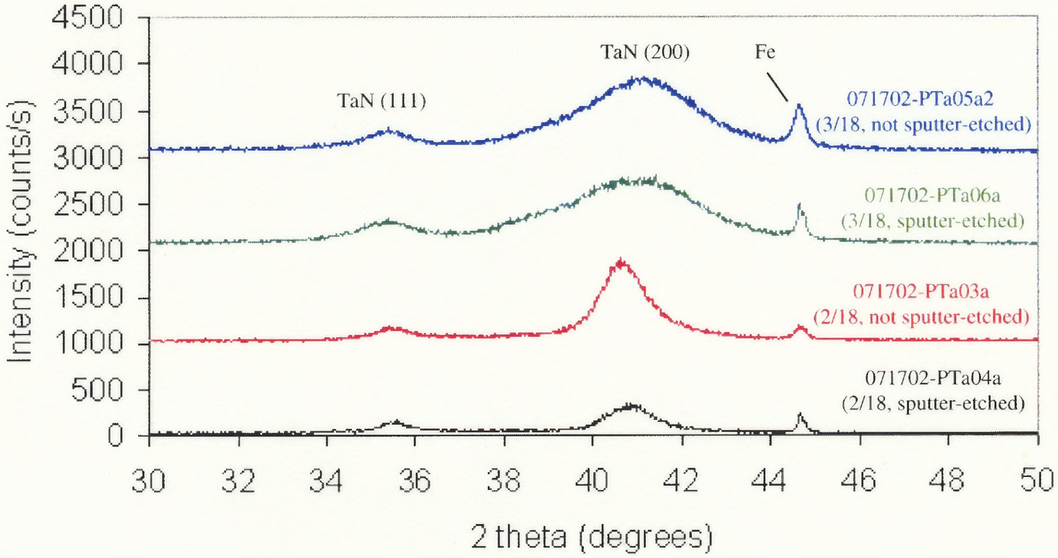

Figure 7.11 Comparison of XRD patterns of tantalum nitride films (~1 μm) deposited on sputter-etched and not sputter-etched steel substrates, produced in 2/18 and 3/18 flow rates.

In recent experiments it was found out that bcc tantalum coatings were produced on sputter etched steel substrates with ~ 20 nm thick tantalum nitride interlayer deposited in flow rate ratios of 3/18 and 4/18. It suggested that sputter etched substrates require richer nitrogen environments to produce favorable crystallographic orientation of tantalum nitride interlayer on which alpha phase tantalum coatings can be grown.

It was checked if redeposition from the substrate holder and mounting screws, while sputter etching, was causing variation in results with respect to phase composition of tantalum coatings deposited on sputter etched and not sputter etched substrates. A special experiment was planned to answer this query. Steel substrates mounted on substrate holders of three different materials, viz. ceramic, aluminum, and steel were loaded inside the chamber for deposition, other conditions remaining the same. No holder material was expected to redeposit on the steel substrate (072302-PTa02a) mounted on ceramic holder, since ceramic is electrically non-conductive. The steel screw to mount the substrates (with threaded hole on its backside) onto the holder was inserted from the back of the holder, so that no part of it is exposed to the sputter etching plasma. The XRD spectra of the tantalum coatings from this experiment are shown in Figure 7.12. No significant difference in the XRD patterns was seen to blame redeposition of the material from the mounting screws or holders for the observed beta phase in tantalum coatings in the sputter-etched samples. The deposition parameters for samples 072302-PTa01a, 072302-PTa02a and 072302-PTa03a were identical (refer to Appendix B).

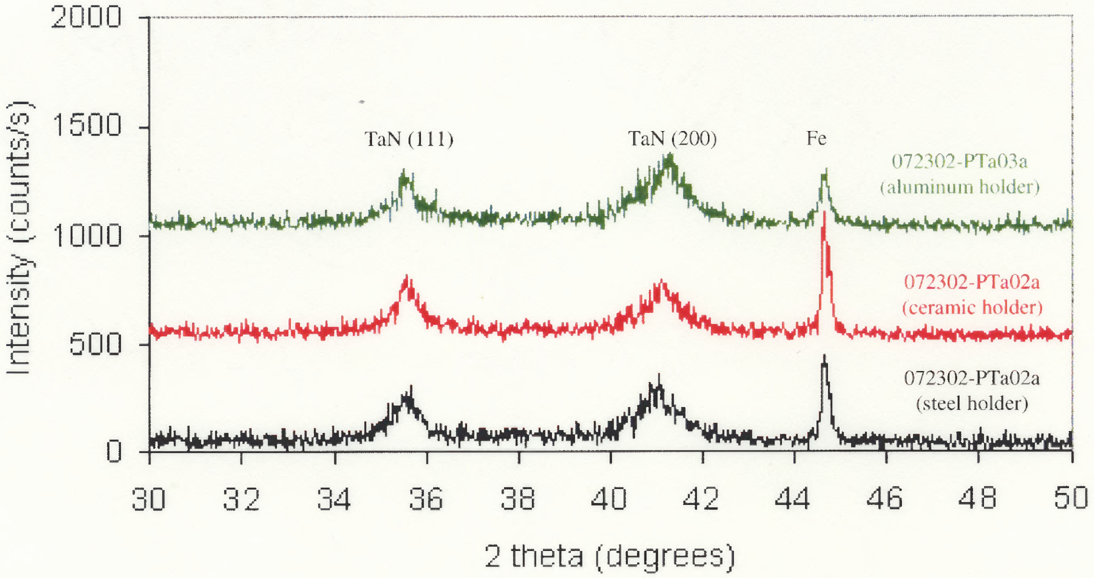

Figure 7.12 Comparison of XRD spectra of tantalum nitride coatings on steel substrates mounted on steel, ceramic and aluminum holders.

7.3 Study of Coating Morphology

Before going any further with results and discussion, a parameter - 'alpha phase ratio', is defined, to indicate the phase composition of the tantalum coatings.

Alpha Phase Ratio

Alpha phase ratio is the ratio of the relative height of most intense α-peak to the sum of the relative heights of the most intense α-peak and β-peak.

$$\text{Alpha phase ratio} = I_\alpha / (I_\alpha + I_\beta) \tag{7.1}$$

where, I_α = relative height of most intense α-peak, and

I_β = relative height of most intense β-peak.

In case of coatings on heated substrates, I_α corresponds to relative height of (222) peak whereas, for coating with tantalum nitride interlayer I_α corresponds to (110) peak height. In both cases, the intensity of (002) β-peak is the highest; hence I_β corresponds to the relative height of (002) peak. From equation 7.1, pure alpha coatings have alpha phase ratio of 1.00, pure beta coatings have alpha phase ratio of 0.00 and mixed phase coatings have values between 0.00 and 1.00. It should be noted, however, that the alpha phase ratio does not represent the relative volumes of the two phases in the coatings. Sample 021102-PTa01a4 shown in Figure 7.14 has alpha phase ratio of 0.05 but still the predominant phase observed in the coating is alpha phase.

The physical distribution of phases in a thick coating having alpha and beta (mixed) phases was observed in the cross-sectional and plan views by an optical microscope with 400X magnification. Matson et al. observed a thin, irregular light-colored beta phase at the coating-substrate interface that changed to a darker alpha phase closer to the coating surface in some thick tantalum coatings [7]. In the thick coatings deposited at NJIT, this kind of phase distribution was not observed. Figure 7.13 shows the cross-sectional view of a thick Ta coating (~ 45 μm) deposited on steel substrate with a nitrided tantalum interlayer. Needle-shaped beta-phase inclusions (light-colored) were found to grow in alpha phase (darker phase). Figure 7.14 is a photomicrograph of the surface of this tantalum coating after fine-grade (0.05 μm) polishing. The light-colored beta phase was seen as white patches on the darker alpha-phase background. The small black spots in Figure 7.14 are inclusions incorporated into the coating during polishing.

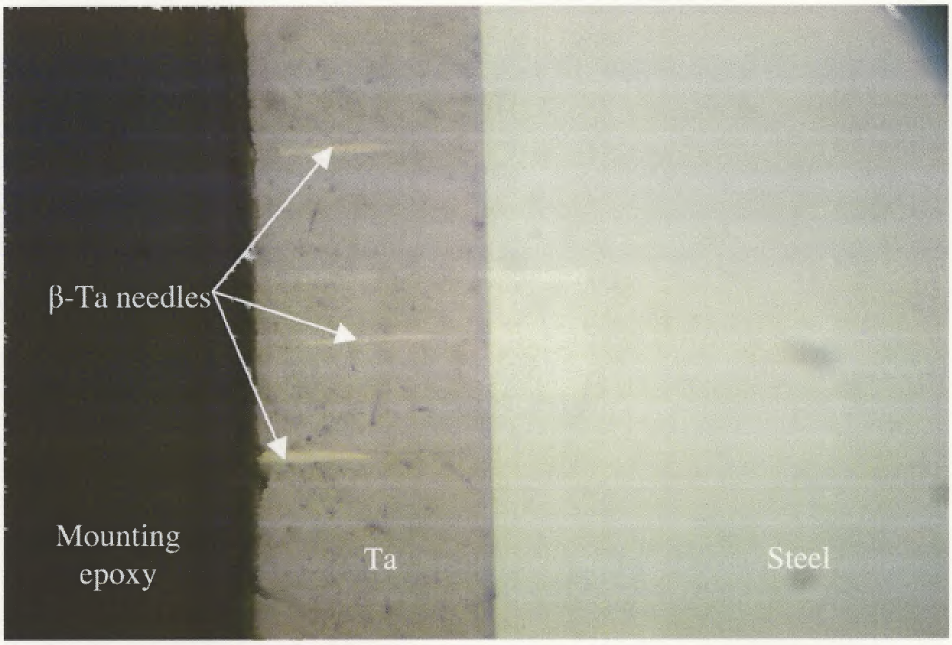

Figure 7.13 Photomicrograph of sputter-deposited tantalum coating on steel substrate with argon sputtering gas. Coating thickness - 45 μm (Sample 021102-PTa01a4).

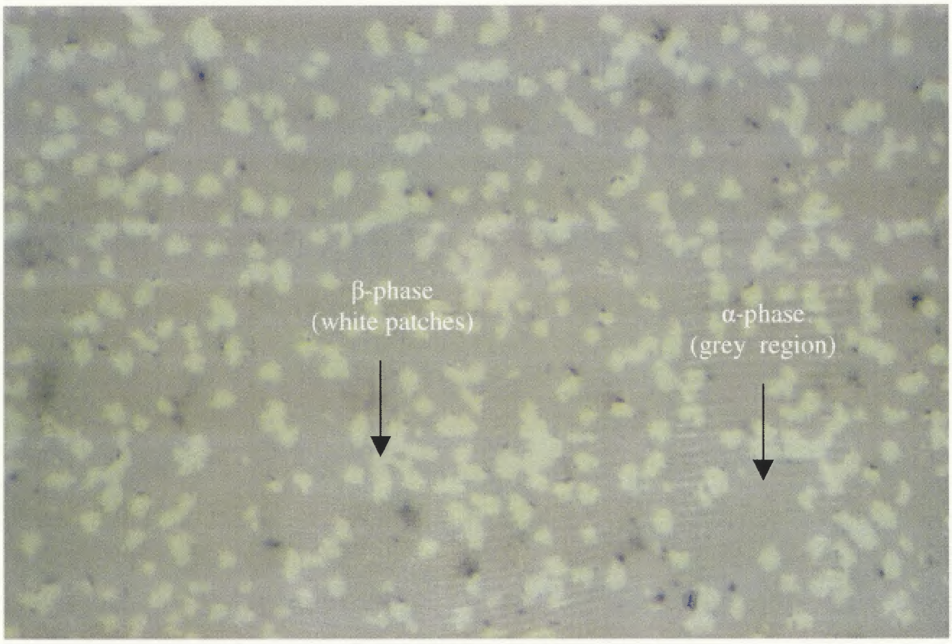

Figure 7.14 Photomicrograph of polished surface of tantalum coating deposited on steel substrate with Ar sputtering gas (Sample 021102-PTa01a4).

SEM study was performed using Environmental Scanning Electron Microscope (ESEM) from Electroscan at NJIT and another instrument in Benet Laboratories. The surface morphology of thick tantalum coating samples is seen in Figure 7.15 and Figure 7.16. In sample 021102-PTa01a2 (alpha phase ratio – 0.81), tantalum coating was deposited on sputter etched substrate, whereas in sample 021902-PTa01a4 (alpha phase ratio – 1.00), coating was deposited without sputter etching of the substrate. The similarity in the topographic features of the two samples suggests similar structure and density of the coatings, although, the phase composition of the two samples is different. It suggests that the bulk of the film, which follows its surface morphology is alpha phase with some beta phase inclusions. Because of the high intensity of the beta peaks in XRD spectrums, alpha phase ratio of 0.81 consists of only small volume of beta inclusions in the film.

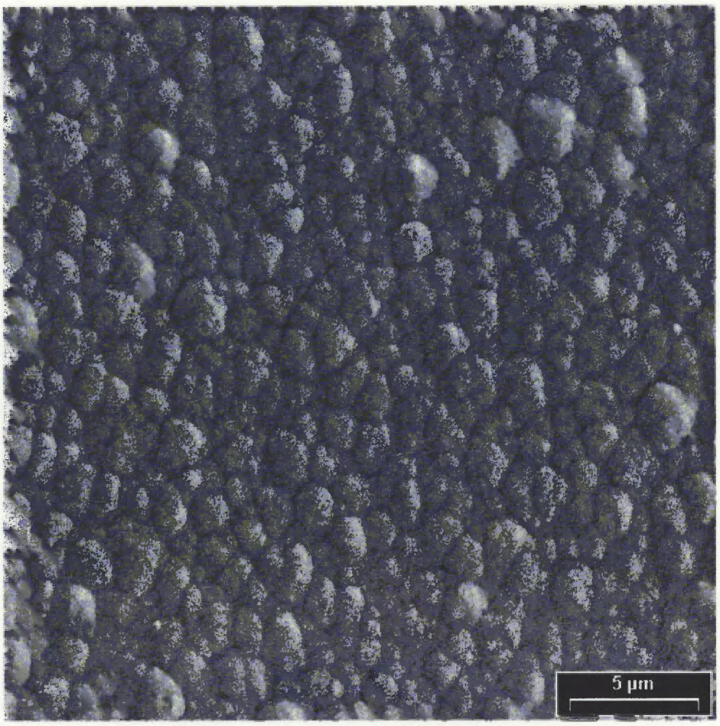

Figure 7.15 Scanning electron micrograph of growth surface of sample 021102-PTa01a2 (on sputter etched substrate), 4,000X.

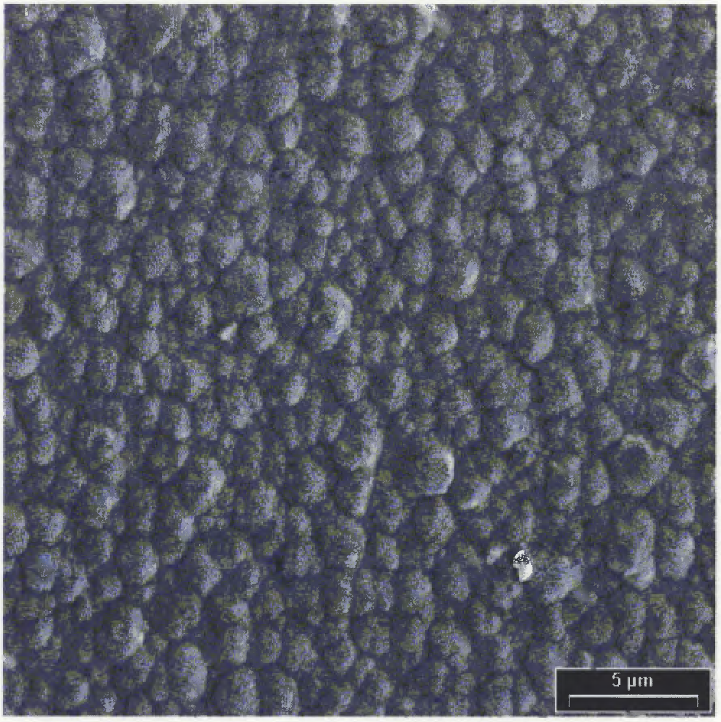

Figure 7.16 Scanning electron micrograph of growth surface of sample 021902-PTa01a4 (on not sputter etched substrate), 4,000X.

7.4 Adhesion Test Results

Adhesion testing of tantalum coatings deposited on steel substrate and on tantalum nitride interlayer was performed using Revetest automatic scratch tester. As discussed in Chapter 6, for comparison of results from various samples, the intrinsic parameters affecting the adhesion test are kept constant though extrinsic parameters may vary from sample to sample. The loading rate of scratching tip of 10 N/min and scratching speed of 1 mm/min was used for all the tests. Thus, the ratio of loading rate to scratching speed (dL/dx) was 10 N/mm. The thickness of tantalum coating on all samples scratched was between 5 μm and 6 μm. The critical load, which is a measure of adhesion strength of the coating, was determined from the product of measured scratch length (where the film failure has initiated) and dL/dx ratio. The film failure for this study was defined as the point where the film has delaminated from the substrate, thus exposing the steel beneath. The film failure was detected by examination with the attached optical microscope in the scratch tester. Discussion of the coating failure and morphology of the scratch channel is given in Section 7.4.2.

7.4.1 Critical Load Measurement

The tantalum coatings used for this study were deposited with two conditions; (i) with a tantalum nitride interlayer deposited on steel substrate, prior to tantalum deposition at room temperature, and (ii) with heating the bare steel substrate during deposition.

Samples with Nitrided Tantalum Interlayer

Table 7.1 lists the critical load values determined for a 5 μm thick tantalum nitride film and four other alpha and beta phase tantalum coatings deposited on nitride interlayer on steel substrates. For deposition conditions used refer to Appendix B. The test results show that a α-phase coating has a better adhesion on the sputter-etched substrate with tantalum nitride interlayer (sample 022502-PTa02a); while for pure β-phase coatings, not sputter-etched substrate (sample 100801-PTa0a) gives better adhesion. Hence, the critical load value depends on both - the phases present in the tantalum coating and the surface treatment of the substrate, that is, sputter-etched or not sputter-etched. From the test results summarized in Table 7.1, alpha phase coatings have much better adhesion than beta phase coatings.

Table 7.1 Critical Load Values Measured for Coatings with Nitride Interlayer

Sample	Surface polish (microns)	Alpha phase ratio	Critical Load (N)	Type of coating
061102-PTa07a2	0.05	~	16.37	TaN
012902-PTa03a1	1	1.00	14.40	α-Ta with TaN (without sputter-etching)
100801-PTa02a	0.5	0.00	14.37	β-Ta with TaN (without sputter-etching)
022502-PTa02a	0.05	1.00	21.80	α-Ta with TaN (sputter-etched)
031202-PTa05a2	0.05	0.00	9.75	β-Ta with TaN (sputter-etched)

In Figure 7.17, critical load values obtained for samples with tantalum nitride interlayer are plotted against the sputtering gas pressure measured on 14 samples (see Appendix C). The flow rate of argon sputtering gas was 18 sccm for all samples. All the samples were sputter etched for time ranging from 10 to 60 minutes. In Figure 7.17, the red colored diamonds represent alpha phase coatings (alpha phase ratio = 1.00), yellow circles are representing predominantly alpha phase coatings (1.00 > alpha phase ratio ≥ 0.90) and blue squares are representing mixed phase coatings (0.90 > alpha phase ratio > 0.00). It is evident from this graph that sputtering gas pressure has a significant impact on the critical load values of tantalum coatings deposited on tantalum nitride interlayer on sputter etched steel substrates. It can be said that lower sputtering gas pressure (1 mtorr) gave better adhering tantalum coatings (critical load was 16.2 N ± 3.7 N) than samples deposited at higher sputtering pressure (5 mtorr). The critical load values for the coatings deposited at 5 mtorr ranged from 7.4 N ± 0.9 N. Alpha phase coatings show relatively higher critical load values at 1 mtorr, though at 5 mtorr the phase composition of the coatings do not influence the critical load values.

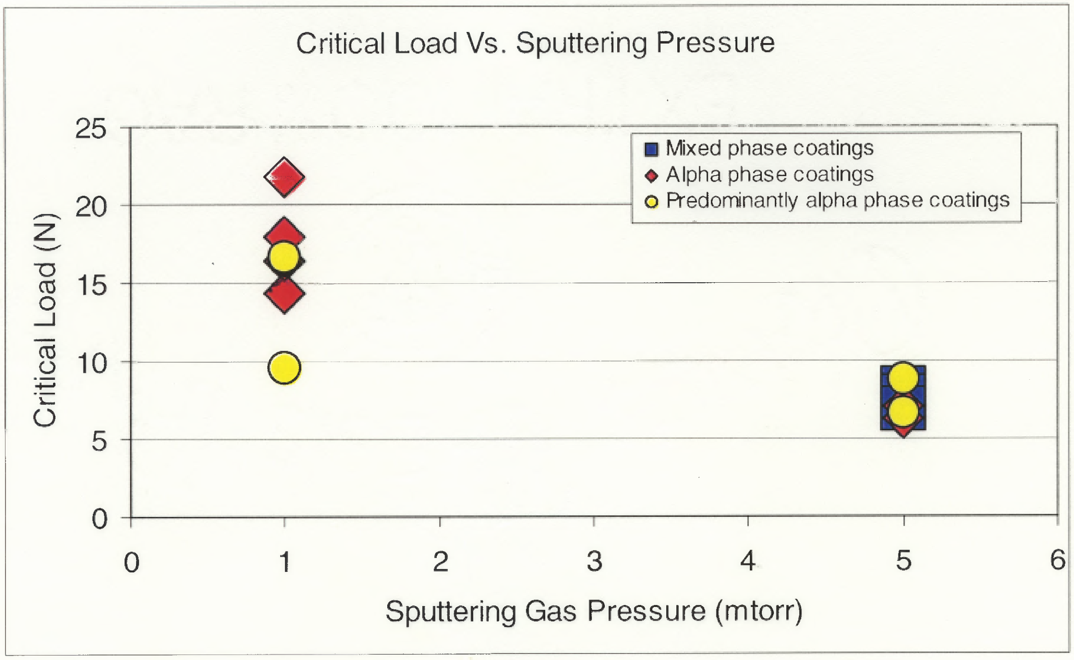

Figure 7.17 Graph of critical load vs. sputtering gas pressure used for tantalum deposition. All the samples were sputter etched and had nitride interlayer (refer to Appendix C).

Four thick tantalum coating samples (thickness > 45 μm) deposited on nitrided interlayer were sent to Benet Laboratories for adhesion testing. Nitride interlayer in samples 021102-PTa01a1 and 021102-PTta01a2 was deposited after 20 minutes of sputter etching the substrate, whereas in 021902-PTta01a3 and 021902-PTa01a4, it was deposited on not sputter etched substrates. The scratch tester employed for this test had a tungsten carbide toolbit in the form of a knife-edge, which ploughed through the coating, completely delaminating the coating at points with poor adhesion. The results showed that coatings on sputter etched substrates had excellent adhesion (Figure 7.18), while gross delamination was observed in coatings on not sputter etched substrates (Figure 7.19). In Figure 7.18, minor adhesive failure at the edge of the sample was observed. It could be due to irregularity in the coating in that region of the sample where a screw held it to the substrate holder.

It was concluded from the adhesion test results of NJIT and Benet Laboratories, that sputter etching improves the adhesion of tantalum coatings. In this study, 20 minutes was found to be optimum time for sputter etching with current density of ~ 25 μA/cm^2 for steel substrates. Pure alpha-phase coatings having critical load more than 15 N were generally considered good coatings with respect to adhesion property, while coatings with mixed phases had poor adhesion.

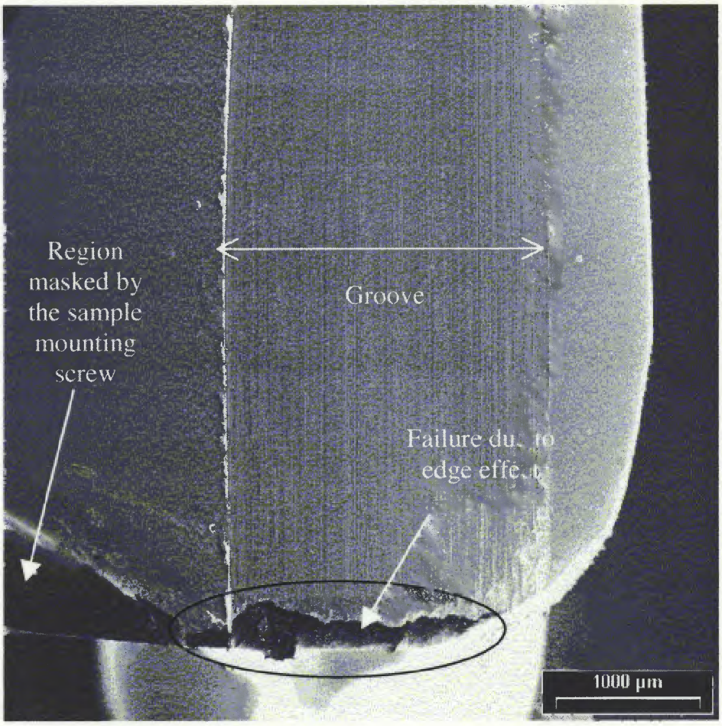

Figure 7.18 Example of a groove produced in a thick coating (~ 45 μm) with excellent adhesion (sample 021102-PTta01a2). The test was performed at Benet Laboratories with a knife-edge type toolbit.

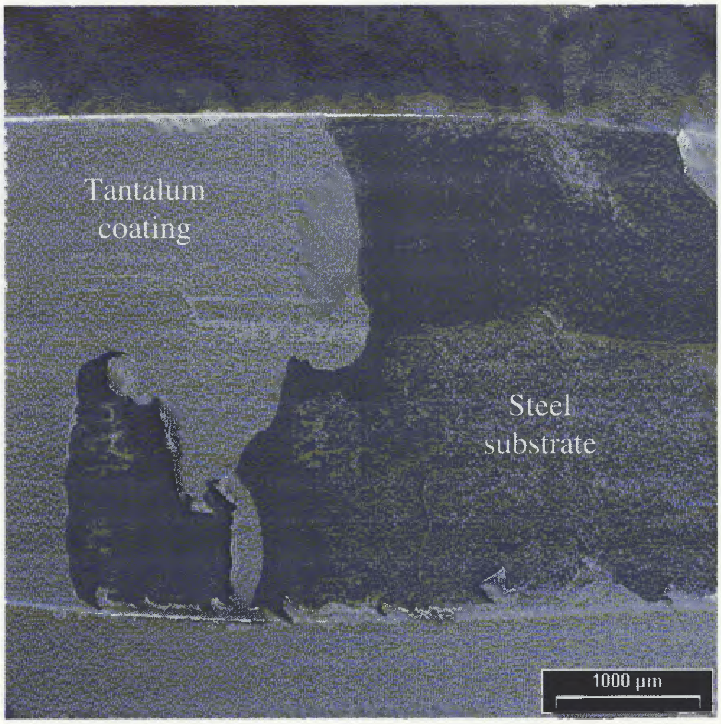

Figure 7.19 Example of groove produced in a thick coating (~ 47 μm) with poor adhesion (sample 021902-PTa01a4). The test was performed at Benet Laboratories with a knife-edge type toolbit.

Samples Prepared with Heated Substrates

The effect of surface preparation by polishing, on adhesion of tantalum coatings and on the phase of the coatings, was also studied. All coatings for this study were deposited on bare steel substrates, which were heated to 300°C or higher, during deposition with argon sputtering gas. Table 7.2 lists the critical load values measured against abrasive particle size used for final polishing. The critical load values in this study ranged from 7.3 N to 12.5 N. The alpha phase ratio is also calculated for each sample coating. In case of substrates polished up to 0.05 μm, pure alpha phase was seen in one run, while in another trial pure beta phase was observed in the coating, under similar deposition conditions. Almost pure alpha was yielded on 268 μm grit polished steel substrates (samples 053102-

PTa04a1 and 070902-PTa07a1) as well as substrates polished up to 0.5 μm grit, whereas, mixed phase was detected in other tantalum coatings. Steinmann et al. [33] had observed that the critical load values for PVD TiN coatings on high speed steel substrate increase with decrease in surface roughness obtained by substrate preparation prior to deposition. In this study, it was noted that critical load was not dependent on the surface preparation by polishing. Hence, it was concluded from the limited results that degree of polishing of steel does not influence the critical load values as well as the phase deposited in the final tantalum coatings.

Table 7.2 Adhesion Test Results for Coatings Deposited on Heated Steel Substrates

Sample	Polishing Abrasive (microns)	Pressure (mtorr)	Flow Gas (sccm)	Power (Watt)	Temp (degree Centigrade)	Time (min)	Estimated thickness (microns)	Phase ratio	Avg. Critical Load (N)
053102-PTa04a1	268	5	18Ar	162.5	300	60	5.4	0.94	10.77
070902-PTa07a1	268	1	18Ar	137.5	300	62	5.6	0.92	12.50
053102-PTa04a2	16	5	18Ar	162.5	300	60	5.4	0.27	7.37
053102-PTa04a3	6	5	18Ar	162.5	300	60	5.4	0.81	7.85
053102-PTa04a4	1	5	18Ar	162.5	300	60	5.4	0.61	8.65
070902-PTa07a2	0.5	1	18Ar	137.5	300	62	5.6	0.95	8.80
070902-PTa07a3	0.05	1	18Ar	137.5	300	62	5.6	1.00	10.70
053102-PTa04a5	0.05	5	18Ar	162.5	300	60	5.4	0.00	10.37

Acoustic emission from the failure region of the coatings was measured during adhesion tests. The sensitivity of the acoustic emission detection meter was set to five units (on a scale of 20 units) for all measurements. It was observed that strong acoustic signals were emitted only from brittle, β-tantalum coatings. No significant signal was emitted from ductile α-tantalum coatings. In some scratch tests, the critical load value measured by optical microscope could be confirmed from the plot of applied normal force versus acoustic signal. The critical load is compared with the load value at which there is a sharp increase in intensity of acoustic emission. Measurement of the coefficient of friction during adhesion testing also can be exploited to find the exact point of film failure. Coefficient of friction was calculated as a ratio of the measured tangential force to the vertical force (load) applied by the tip to the coating. The coefficient of friction between scratching diamond tip and tantalum film and that between tip and steel substrate is different. At the point where a sharp change in the coefficient of friction value is observed, the applied normal force was taken as the critical force for adhesion. In Figure 7.20 the applied normal force is plotted against double Y-axes. On left hand side is acoustic emission and on right hand side is frictional coefficient. The critical load value obtained for sample 053102-PTa04a5 by optical microscope examination was 9.6 N, which is comparable with critical load values obtained from acoustic emission (9.3 N) and coefficient of friction (9.5 N) plots in Figure 7.20. There was no such close correlation between these three measurements in most other samples.

In ductile α-Ta coatings, no acoustic emission was detected even where the film had failed under high applied force. At times, coating was not removed from below the tip even after delamination from the substrate and hence change in coefficient of friction was not registered. Critical load values obtained from acoustic signal and coefficient of friction modes in such cases can be only considered complementary to the critical load values obtained by optical microscopy mode, which is the most reliable method to judge the adhesion failure of α-Ta coatings.

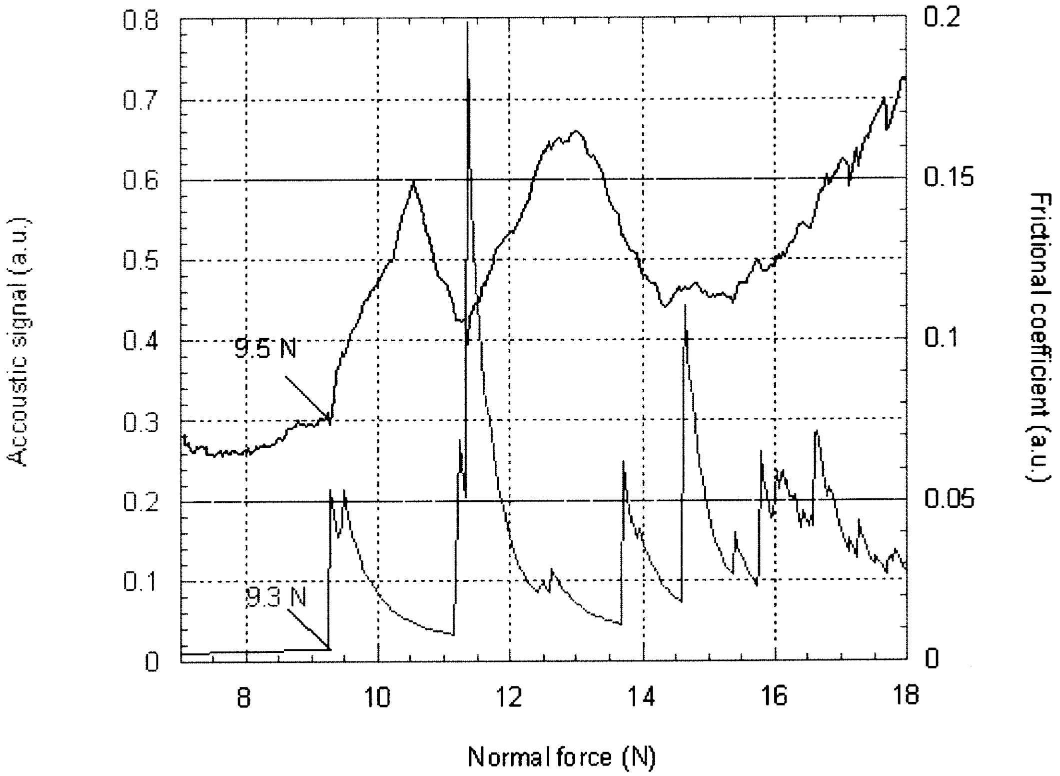

Figure 7.20 Acoustic signal (bottom curve) and frictional coefficient (top curve) plotted against the applied normal force for β-Ta coating (sample 053102-PTa04a5). The microscopic examination revealed the critical failure at 9.6 N.

7.4.2 Modes of Film Failure

Two distinct types of film failure were observed under an optical microscope during the adhesion test. Failure mode depended on the phases present in the tantalum coatings. In case of β-Ta coatings, cracks were induced perpendicular to the scratching direction and also at an angle to, and outside, the scratch channel, signifying the brittle nature of beta tantalum. Delamination and hence, exposure of steel substrate is often outside the scratch channel for such tantalum coatings. Figure 7.21 shows a photomicrograph of a typical failure in β-Ta coating. Generally, no difference in failure pattern of β-Ta coating deposited on sputter etched or not sputter etched steel substrates was observed. One particular scratch pattern on β-Ta coating (sample 031202-PTa05a2) was unusual (see Figure 7.22). Angular cracks outside of the scratch channel, generally observed in β-Ta coatings were missing in this case. Major cracking and finally film failure (substrate exposure) was observed inside the channel.

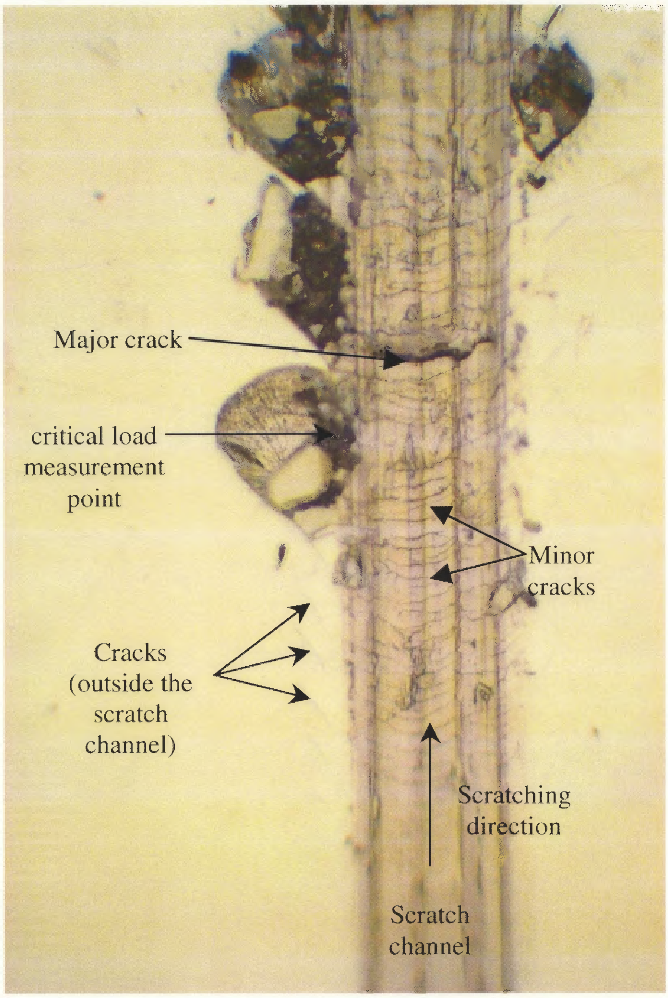

Figure 7.21 Scratch channel observed in β-Ta coating (sample 100801-PTa02a, deposited on ~0.3 μm thick nitride interlayer, without sputter etching the substrate), critical load – 14.37 N.

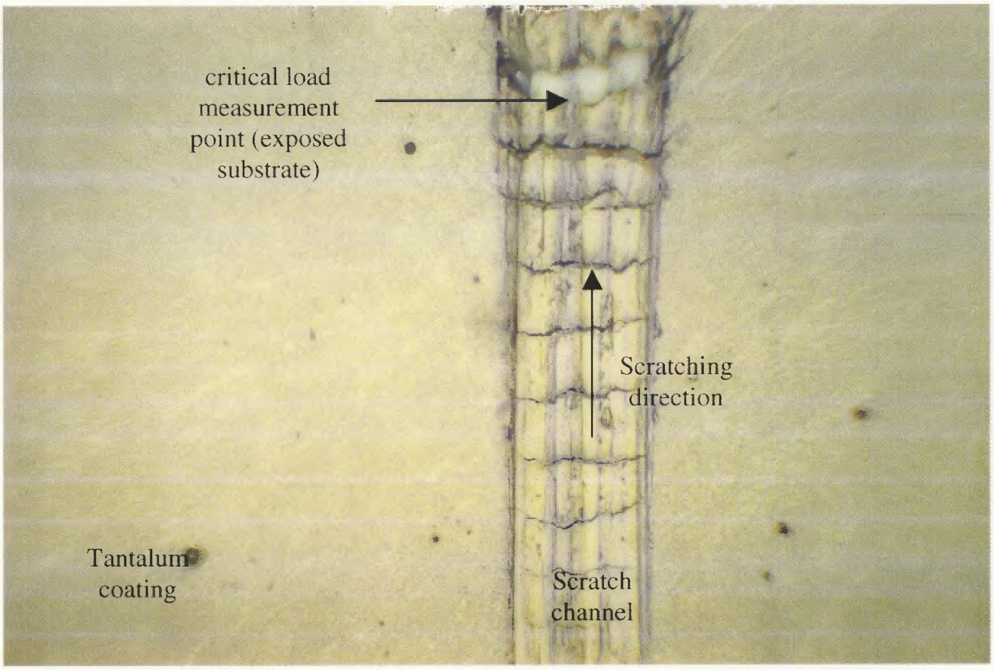

Figure 7.22 Coating failure pattern observed in β-Ta coating (sample 031202-PTa05a2, deposited on ~20 nm thick nitride interlayer (2/18), after sputter etching the substrate), critical load – 9.75 N.

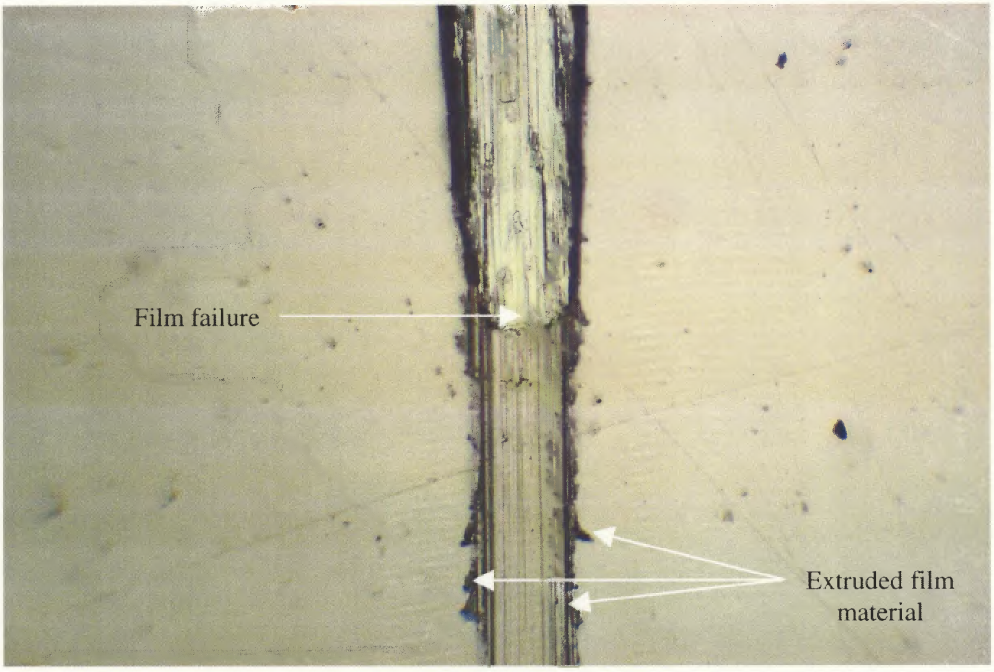

Figure 7.23 Scratch pattern of α-Ta coating (sample 012902-PTa03a1 - deposited on 20 nm thick nitrided tantalum interlayer, on sputter etched substrate), critical load – 14.40 N.

Photomicrograph shown in Figure 7.23 represents a typical scratch pattern for tantalum coatings having pure α-phase (sample 012902-PTa03a1). The coating material was extruded and pulled along with the scratching diamond tip. The extruded material was also pushed to the sides of the scratch channel forming hillocks. No cracks were observed inside or around the scratch channel in this sample. The film failed at a definite point exposing the steel substrate below it, without prior cracking. No acoustic signal was detected during the test. This type of film failure can be explained by the ductile nature of bcc tantalum. Coatings having mixed phase showed scratch channel and film failure similar to observed in coatings with pure alpha phase (Figure 7.24). This can be explained by the fact that there is significant volume of α-phase in the film (refer to Figure 7.14), which provides the necessary ductility to avoid cracking.

Figure 7.25 represents a scratch channel made in tantalum nitride film. The failure, characteristic of a brittle material was accompanied by acoustic emission in this case. The critical load (> 15 N) was considered high, signifying good adhesion between the nitride film and the sputter etched steel substrate. It suggests that the adhesive failure of the beta phase coatings on nitride interlayers might have occurred on the Ta - TaN interface rather than on the TaN - steel interface.

Microscopic examination of the modes of failure of alpha and beta tantalum coatings reveal that the critical load may not be a good measure of the coating performance in applications, where they are subjected to mechanical stresses in a corrosive environment. Small cracks appearing in the beta phase coatings below the critical load will lead to exposure of the substrate to the corrosive environment and subsequent failure of the protective coatings.

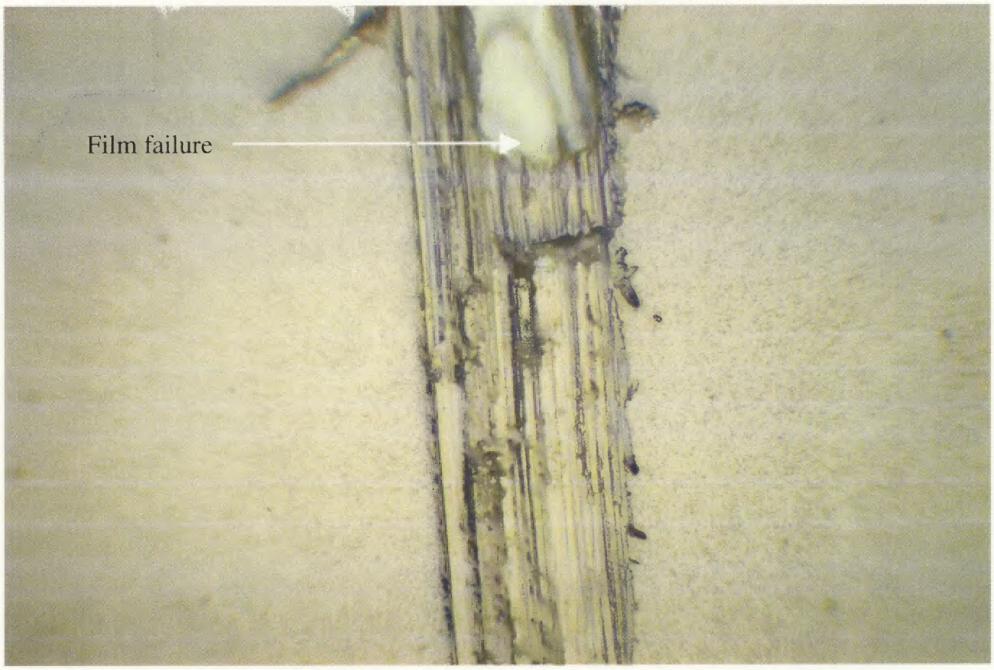

Figure 7.24 Scratch pattern of mixed phases coating (sample 052202-PTa02a - with 10 nm thick nitride interlayer on sputter etched substrate, alpha phase ratio – 0.30), critical load – 7.75 N.

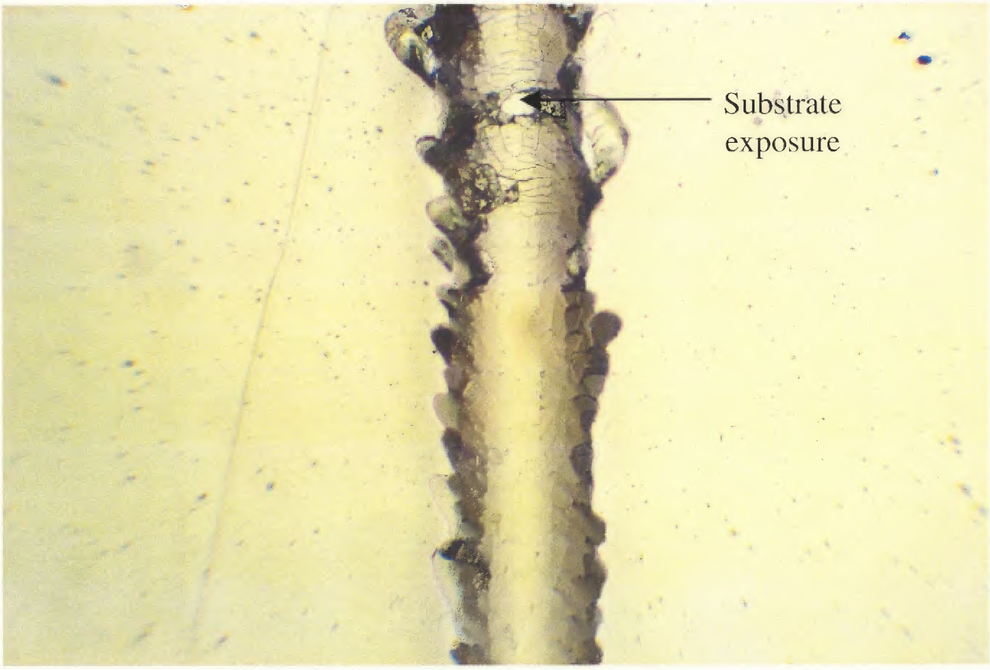

Figure 7.25 A typical scratch channel made in nitrided tantalum film deposited on sputter etched steel substrate (Sample 061102-PTa07a2, critical load – 16.37 N).

CHAPTER 8

CONCLUSIONS

The tantalum coatings studied in this work were produced by DC magnetron sputtering process at NJIT. Tantalum coatings were deposited with three different conditions -

- Deposition on bare steel at room temperature
- Deposition on bare steel heated to elevated temperature
- Deposition on tantalum nitride interlayer deposited on steel prior to tantalum coating

The following conclusions can be drawn from the results of these experiments.

Tantalum Phase

- Tetragonal β-phase or mixed phases, bcc-phase (α-phase) and β-phase, were observed in coatings deposited on bare steel at room temperature with argon and krypton sputtering gases.
- Alpha phase tantalum coatings on steel were obtained by heating the substrates above a threshold temperature. For argon sputtering gas, this threshold temperature is between 350°C and 400°C, while for krypton sputtering gas, this temperature is expected to be approximately 50°C lower. A more precise determination of the two threshold temperatures is carried out in the ongoing experiments.
- Tantalum coatings with pure α-phase were also obtained by deposition on tantalum nitride interlayer (grown by reactive sputtering in a mixture of argon and nitrogen gases), which was deposited on steel substrate prior to tantalum deposition at room

temperature. The minimum thickness of the nitride interlayer necessary for yielding pure α-phase tantalum coatings was estimated at 20 nm.

Nitride Interlayer

- X-ray diffraction and nuclear reaction analysis studies showed that pure α-phase tantalum was deposited at room temperature only on interlayers of the stoichiometric tantalum nitride (TaN). This supports the hypothesis that bcc-phase of tantalum grows epitaxially on fcc TaN crystals.
- The ratio of nitrogen to argon flow rates during reactive sputtering determines the composition of the deposited nitride layer. The stoichiometric TaN was grown for the nitrogen to argon flow rate ratios of 2/18, 3/18, 4/18, 5/18 and 7/18. Tantalum deposited on nitride interlayers grown at lower nitrogen flow rate (1/18) consists of mixed or beta phases. At the flow ratio of 1/30, hexagonal Ta_2N was observed in the nitride film.

Adhesion of Tantalum Coatings

Adhesion was measured by the critical load on the diamond tip, moving across the coating surface, required to delaminate the coating from the substrate, as observed by an optical microscope. Acoustic emission from the test sample and, in some cases, the lateral force was also measured during the scratch test.

- Two distinct modes of failure were observed in tantalum coatings depending on the phase composition of the coatings.

  - The beta-phase coatings showed brittle failure with cracks propagating in and around the scratch channel. The failure of brittle films was usually accompanied by acoustic emission.
  - The alpha phase coatings and coatings with mixed phases showed ductile failure under the stresses applied by the scratching tip. No cracking was detected in such coatings prior to complete delamination of the coating from the substrate and there was no measured acoustic signal from the failure of such coatings.

- The coatings having high critical load values (> 15 N) were predominantly alpha phase coatings.
- Sputter etching of the steel substrate prior to a nitride interlayer deposition improves the adhesion. *This was concluded from the groove adhesion testing at Benet Laboratories of two thick tantalum coatings.*
- For α-tantalum coatings deposited on tantalum nitride interlayer, the sputtering gas pressure had a strong influence on the critical load values. Tantalum coatings produced at 1 mtorr sputtering gas pressure had better adhesion than coatings produced at 5 mtorr pressure. This conclusion cannot be extended to coatings produced on heated substrates, due to limited testing.
- For coatings deposited on heated substrates, the size of the polishing abrasive used (and hence, the surface roughness of the substrate prior to deposition process), did not influence the critical load value or the phase composition of the coatings.

APPENDIX A

STANDARD POWDER DIFFRACTION PATTERNS FOR α-TANTALUM AND β-TANTALUM

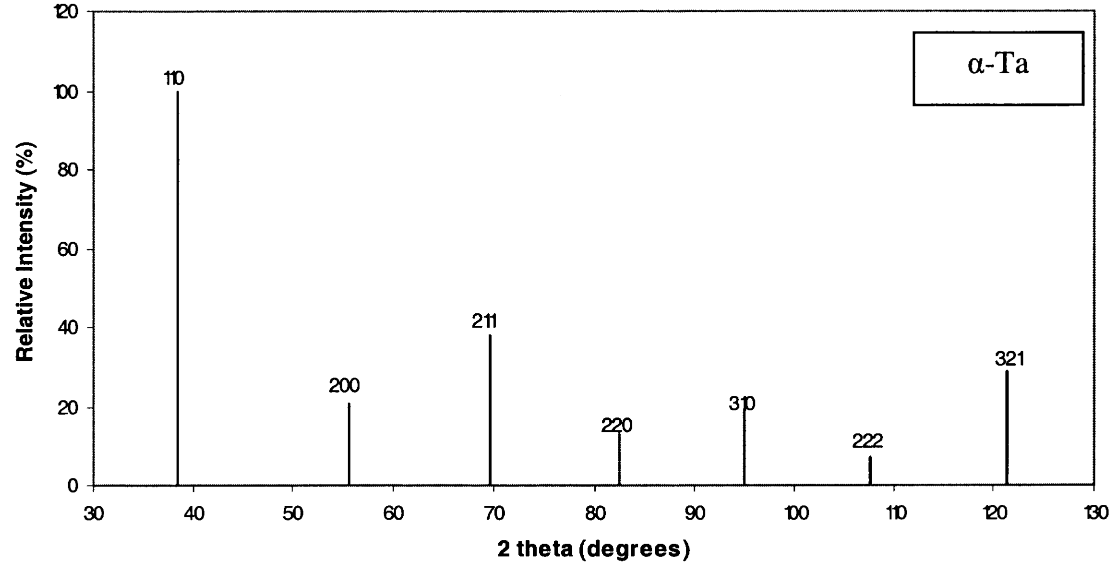

Figure A1 Standard powder diffraction spectrum of bcc-tantalum (JCPDS Ref. Card No. 04-788)

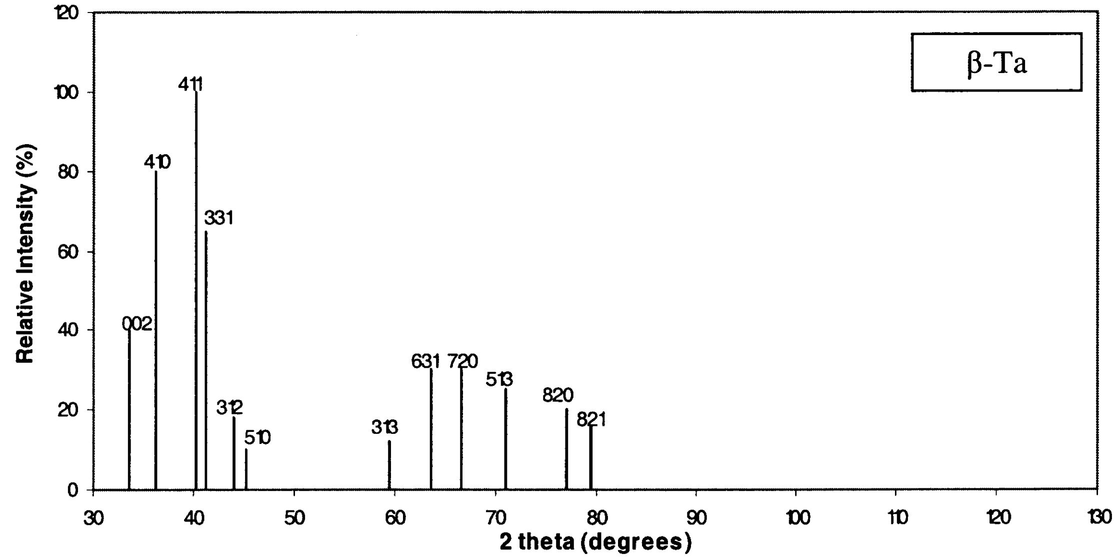

Figure A2 Standard powder diffraction spectrum of β-tantalum (JCPDS Ref. Card No. 25-1280)

APPENDIX B

DETAILS OF DEPOSITION CONDITIONS

Table B1 Details of Deposition Conditions of Samples Discussed in the Thesis

(TS – row refers to deposition conditions during tantalum sputtering, RS- row refers to deposition conditions during reactive sputtering, SE- row refers to conditions during sputter etching)

Sample	Surface Polish (microns)	Conditions during	Pressure (mtorr)	Gas Flow (sccm)	Power (W)	Temp (°C)	Time (min)	Phase
071901-PTa01a	15	TS	23	18Ar	300	250	10	mixed
081601-PTa01a1	15	TS	1.1	1.5Kr	160	RT	120	β
081601-PTa03a	15	TS	1.1	1.5Kr	152	250	30	
082401-PTa02a	15	TS	1	1N/1.5Ar	112.5	RT	120	mixed
082401-PTa05a	15	TS	1	1Ar	135	300	30	α
100801-PTa02a	0.5	RS	5	1N/6Ar	175	RT	10	
		TS	5	2.8Ar	162.5	RT	60	β
101901-PTa02a	0.5	RS	5.7	5N/18Ar	175	RT	15	Nitride
101901-PTa03a	0.5	RS	4.6	4N/18Ar	200	RT	15	Nitride
112101-PTa04a1	0.05	RS	5	1N/30Ar	200	RT	27	Nitride
012902-PTa03a1	1	RS	5	3N/18Ar	165	RT	0.25	
		TS	5	18Ar	200	RT	60	α
020502-PTa02a	0.5	RS	5	2N/18Ar	225	RT	0.08	
		TS	5	18Ar	175	RT	20	α
020502-PTa03a	0.5	RS	5	3N/18Ar	225	RT	0.13	
		TS	5	18Ar	175	RT	20	α
021102-PTa01a1	0.05	SE	200	18Ar		RT	20	
		RS	5	2N/18Ar	175	RT	0.25	
		TS	1.1	18Ar	185	RT	480	α
021102-PTa01a2	0.05	SE	200	18Ar		RT	20	
		RS	5	2N/18Ar	175	RT	0.25	
		TS	1.1	18Ar	185	RT	480	mixed
021102-PTa01a4	0.05	SE	200	18Ar		RT	20	
		RS	5	2N/18Ar	175	RT	0.25	
		TS	1.1	18Ar	185	RT	480	mixed
021902-PTa01a3	0.05	RS	5	2N/18Ar	200	RT	0.25	
		TS	1	18Ar	200	RT	491	α
021902-PTa01a4	0.05	RS	5	2N/18Ar	200	RT	0.25	
		TS	1	18Ar	200	RT	491	α
022502-PTa02c		SE	195	18Ar		RT	20	
		RS	5	2N/18Ar	195	RT	0.33	
		TS	1	18Ar	175	RT	60	

APPENDIX B

Table B1 Details of Deposition Conditions of Samples Discussed in the Thesis (Continued)

Sample	Surface Polish (microns)	Conditions during	Pressure (mtorr)	Gas Flow (sccm)	Power (W)	Temp (°C)	Time (min)	Phase
022502-PTa02a	0.05	SE	195	18Ar		RT	20	
		RS	5	2N/18Ar	195	RT	0.33	
		TS	1	18Ar	175	RT	60	α
031202-PTa05a2	0.05	SE	215	18Ar	0.3	RT	40	
		RS	5	2N/18Ar	230	RT	0.33	
		TS	1	18Ar	200	RT	60	β
052202-PTa02a	0.05	SE	225	18Ar	0.4	RT	20	
		RS	5	2N/18Ar	212.5	RT	0.17	
		TS	5	18Ar	175	RT	60	mixed
061102-PTa07a2	0.05	SE	225	18Ar	0.5	RT	20	
		RS	5	2N/18Ar	185	RT	60	Nitride
071702-PTa03a	0.05	RS	5	2N/18Ar	160	RT	20	Nitride
071702-PTa04a	0.05	SE	225	18Ar	0.4	RT	20	
		RS	5	2N/18Ar	160	RT	20	Nitride
071702-PTa05a2	0.05	RS	5	3N/18Ar	170	RT	20	Nitride
071702-PTa06a	0.05	SE	225	18Ar	0.3	RT	20	
		RS	5	3N/18Ar	170	RT	20	Nitride
072302-PTa01a	0.05	SE	225	18Ar	0.2	RT	20	
		RS	5	2N/18Ar	150	RT	20	Nitride
072302-PTa02a	0.05	SE	225	18Ar	0.2	RT	20	
		RS	5	2N/18Ar	150	RT	20	Nitride
072302-PTa03a	0.05	SE	175	18Ar	0.3	RT	20	
		RS	5	2N/18Ar	150	RT	20	Nitride

APPENDIX C

SPUTTERING DEPOSITION DETAILS OF SAMPLES REPRESENTING THE DATA POINTS IN FIGURE 7.17

Table C1 Sputtering Deposition Details of Samples Representing the Data Points in Figure 7.17

(TS – row refers to deposition conditions during tantalum sputtering, RS- row refers to deposition conditions during reactive sputtering, SE- row refers to conditions during sputter etching)

Sample	Surface Polish (microns)	Conditions during	Pressure (mtorr)	Gas Flow (sccm)	Power (W)	Temp (°C)	Time (min)	Phase	Alpha phase ratio	Critical Load (N)
021902-PTa05a2	0.05	SE	205	18Ar		RT	20			
		RS	5	2N/18Ar	250	RT	0.67			
		TS	1	18Ar	212.5	RT	60	α	1	16.7
021902-PTa06a2	0.05	SE	210	18Ar		RT	20			
		RS	5	2N/18Ar	250	RT	2			
		TS	1	18Ar	215	RT	60	α	1	14.33
022502-PTa01a	0.05	SE	195	18Ar		RT	22			
		RS	5	2N/18Ar	195	RT	0.5			
		TS	1	18Ar	175	RT	60	α	1	17.97
022502-PTa02a	0.05	SE	195	18Ar		RT	20			
		RS	5	2N/18Ar	195	RT	0.33			
		TS	1	18Ar	175	RT	60	α	1	21.8
022502-PTa03a	0.05	SE	195	18Ar		RT	20			
		RS	5	2N/18Ar	195	RT	0.17			
		TS	1	18Ar	175	RT	60	mixed	0.98	16.52
042402-PTa05a1	0.05	SE	225	18Ar	0.9	RT	20			
		RS	5	2N/18Ar	200	RT	1			
		TS	1	18Ar	162.5	RT	60	α	1	16.43
042402-PTa05a2	0.05	SE	225	18Ar	0.9	RT	20			
		RS	5	2N/18Ar	200	RT	1			
		TS	1	18Ar	162.5	RT	60	mixed	0.97	9.57
050302-PTa06a	0.05	SE	225	18Ar	0.6	RT	20			
		RS	5	2N/18Ar	262.5	RT	0.33			
		TS	5	18Ar	180	RT	71	mixed	0.95	8.87
050302-PTa07a	0.05	SE	225	18Ar	0.6	RT	40			
		RS	5	2N/18Ar	262.5	RT	0.33			
		TS	5	18Ar	180	RT	60	α	1	6.25
052202-PTa02a	0.05	SE	225	18Ar	0.4	RT	20			
		RS	5	2N/18Ar	212.5	RT	0.17			
		TS	5	18Ar	175	RT	60	mixed	0.3	7.75

APPENDIX C

Table C1 Sputtering Deposition Details of Samples Representing the Data Points in Figure 7.17 (Continued)

Sample	Surface Polish (microns)	Conditions during	Pressure (mtorr)	Gas Flow (sccm)	Power (W)	Temp (°C)	Time (min)	Phase	Alpha phase ratio	Critical Load (N)
052202-PTa04a	0.05	SE	225	18Ar	0.4	RT	10			
		RS	5	2N/18Ar	212.5	RT	0.17			
		TS	5	18Ar	175	RT	60	mixed	0.47	8.25
052202-PTa05a	0.05	SE	225	18Ar	0.4	RT	40			
		RS	5	2N/18Ar	212.5	RT	0.17			
		TS	5	18Ar	175	RT	60	mixed	0.07	6.93
053102-PTa01a	0.05	SE	225	18Ar	0.4	RT	10			
		RS	5	2N/18Ar	168.8	RT	0.33			
		TS	5	18Ar	135	RT	60	α	1	7.1
053102-PTa02a	0.05	SE	225	18Ar	0.4	RT	60			
		RS	5	2N/18Ar	168.8	RT	0.33			
		TS	5	18Ar	135	RT	60	mixed	0.98	6.63

REFERENCES

1. A. Patel, L. Gladczuk, C. S. Paur and M. Sosnowski, "Sputter-deposited bcc tantalum on steel with the interfacial tantalum nitride layer," *Mat. Res. Soc. Symp. Proc.*, vol. 697, P5.6, 2002.

2. R. J. Gutmann, J. M. Steigerwald, L. You, D. T. Price, J. Neirynck, D. J. Duquette and S. P. Murarka, "Chemical-mechanical polishing of copper with oxide and polymer interlevel dielectrics," *Thin solid Films,* 270, pp. 596-600, 1995.

3. S. L. Lee, D. Windover, M. Audino, D. W. Matson and E. D. McClanahan, "High-rate sputter deposited tantalum coating on steel for wear and erosion mitigation," *Surf. and Coat. Technol.,* 149, pp. 62-69, 2002.

4. W. Ensinger, "Corrosion and wear protection of tube inner walls by ion beam sputter coating," *Surf. and Coat. Technol.*, 86-87, pp. 438-442, 1996.

5. R. Westergard, M. Bromark, M. Larsson, P. Hedenqvist and S. Hogmark, "Mecanical and tribological characterization of DC magnetron sputtered tantalum nitride thin films," *Surf. and Coat. Technol.*, 97, pp. 779-784, 1997.

6. Y. X. Leng, H. Sun, P. Yang, J. Y. Chen, J. Wang, G. J. Wan, N. Huang, X. B. Tian, L. P. Wang and P. K. Chu, "Biomedical properties of tantalum nitride films synthesized by reactive magnetron sputtering," *Thin Solid Films*, 398-399, pp. 471-475, 2001.

7. D. W. Matson, E. D. McClanahan, J. P. Rice, S. L. Lee and D. Windover, "Effect of sputtering parameters on Ta coatings for gun bore applications," *Surf. and Coat. Technol,*. 133-134, pp. 411-416, 2000.

8. P. Shivaramkrishnan, "Characterization of Tantalum Coatings on Steel Substrates", Master Thesis, Department of Materials Science and Engineering, New Jersey Institute of Technology, January 1999.

9. A. J. Perry, C. Béguin and H. E. Hintermann, "The Microstructure of Tantalum Coatings on Mild Steel," *Berna AG*, Olten, Switzerland, pp. 131-139.

10. S. L. Lee, M. Cipollo, D. Windover and C. Rickard, "Analysis of magnetron-sputtered tantalum coatings versus electrochemically deposited tantalum from molten salt," *Surf. and Coat. Technol.*, 120-121, pp. 44-52, 1999.

11. J. F. Cox, and E. D. McClanahan, "High rate sputtering of tantalum onto gun steel," *Proc. of Tri-Service Gun Tube Wear and Erosion Symposium*, 277, 1982.

12. H. Shimada, I. Ohshima, T. Ushiki, S. Sugawa, and T. Ohmi, "Tantalum nitride metal gate FD-SOI CMOS FETs using low resistivity self-grown bcc-tantalum layer," *IEEE Trans. on Electron Devices*, Vol. 48, No. 8, pp. 1619-1626, August 2001.

13. P. Catania, R. A. Roy and J. J. Cuomo, "Phase formation and microstructure changes in tantalum thin films induced by bias sputtering," *Journal of Applied Physics*, Vol. 74, Issue 2, pp. 1008-1014, July 15, 1993.

14. L. A. Clevenger, A. Mutscheller, J. M. E. Harper, C. Cabral, Jr. and K. Barmak, "The relationship between deposition conditions, the beta to alpha phase transformation, and stress relaxation in tantalum thin films," *Journal of Applied Physics* 72 (10), pp. 4918-4924, 15 November 1992

15. D. W. Matson, M. D. Merz, and E. D. McClanahan "High rate sputter deposition of wear resistant tantalum coatings," *Journal of Vacuum Science Technology*, Vol.A 10(4), pp. 1791-1796, July/Aug 1992.

16. S. L. Lee and D. Windover, "Phase, residual stress, and texture in triode-sputtered tantalum coatings on steel", *Surface and Coatings Technology*, 108-109, pp. 65-72, 1998.

17. D. W. Matson, E. D. McClanahan, S. L. Lee, D. Windover, "Properties of thick sputtered Ta used for protective gun tube coatings," *Surface and Coatings Technology,* 146-147, pp. 344-350, 2001.

18. Milton Ohring, *The materials science of thin films*, Academic Press, 1990.

19. Brian Chapman, *Glow Discharge Processes, Sputtering and Plasma Etching*, Wiley-Interscience publication, 1980.

20. I. Ahmad, P. Greco, G. D'Andrea and J. Barranco, " Potential erosion resistant refractory metal (and/or) alloy coatings for gun tubes," *Proc. Of Triservice Conf. on Corrosion*, Battelle Memorial Institute, Columbus, OH, pp. 203, 1978.

21. Metals Handbook, *American Society of Metals*, Desk Edition, ed. H. E. Boyer and T. L. Gall, Chapter 4, 1985.

22. Metals Handbook, *American Society of Metals, Metallography and Microstructures,* Ninth Edition, Volume 9, 1985.

23. Buehler, *Metal Digest - Minimet polisher/grinder*, volume 20, number 1 (operation manual).

24. Metals Handbook, *American Society of Metals, Surface cleaning, Finishing, and Coating,* Ninth Edition, Volume 5, 1982.

25. Kurt J. Lesker Company, *TORUS 1C, 2C, 3M, 4M magnetron sputtering sources, installation and operation manual for vertical, right angle, flex mount models*, second edition, 1994.

26. J. L. Vossen, "The preparation of substrates for film deposition using glow discharge technique," review article, RCA Laboratories, Princeton, NJ, pp. 159-165, 1979.

27. H. P. Klug and L. E. Alexander, *X-ray diffraction procedures, for polycrystalline and amorphous materials*, second edition, Wiley-Interscience Publication, 1974.

28. J. I. Goldstein, D. E. Newbury, P. Echlin, D. C. Joy, A. D. Romig, Jr., C. E. Lyman, C. Fiori and E. Lifshin, *Scanning Electron Microscopy and X-Ray Microanalysis, A text for Biologists, Materials Scientists, and Geologists*, second edition, Plenum Press, 1994.

29. Sidney H. Avner, *Introduction to physical metallurgy*, Second Edition, Tata McGraw-Hill Edition, 1997.

30. http://www.ulg.ac.be/ipne/ipne/iba/IBA.html

31. A. J. Perry, "The adhesion of chemically vapour-deposited hard coatings to steel-the scratch test," *Thin Solid Films*, 78, pp. 77-93, 1981.

32. A. J. Perry, "Adhesion studies of ion-plated TiN on steel," *Thin Solid Films*, 81, pp. 357-366, 1981.

33. P. A. Steinmann, Y. Tardy and H. E. Hintermann, "Adhesion testing by the scratch test method: the influence of intrinsic and extrinsic parameters on the critical load," *Thin Solid Films*, 154, pp. 333-349, 1987.

34. T. Riekkinen, J. Molarius, T. Laurila, A. Nurmela, I. Suni and J.K. Kivilahti, "Reactive sputter deposition and properties of Ta_xN thin films," *Microelectronic Engineering*, 1, 000-000, 2002.

35. http://www.srim.org/